

University of Windsor

## Scholarship at UWindor

---

Electronic Theses and Dissertations

Theses, Dissertations, and Major Papers

---

6-18-2021

# Hypervelocity Impact on Satellite Sandwich Structures: Development of a Simulation Model and Investigation of Projectile Shape and Honeycomb Core Effects

Reihaneh Aslebagh  
*University of Windsor*

Follow this and additional works at: <https://scholar.uwindsor.ca/etd>

---

### Recommended Citation

Aslebagh, Reihaneh, "Hypervelocity Impact on Satellite Sandwich Structures: Development of a Simulation Model and Investigation of Projectile Shape and Honeycomb Core Effects" (2021). *Electronic Theses and Dissertations*. 8589.

<https://scholar.uwindsor.ca/etd/8589>

This online database contains the full-text of PhD dissertations and Masters' theses of University of Windsor students from 1954 forward. These documents are made available for personal study and research purposes only, in accordance with the Canadian Copyright Act and the Creative Commons license—CC BY-NC-ND (Attribution, Non-Commercial, No Derivative Works). Under this license, works must always be attributed to the copyright holder (original author), cannot be used for any commercial purposes, and may not be altered. Any other use would require the permission of the copyright holder. Students may inquire about withdrawing their dissertation and/or thesis from this database. For additional inquiries, please contact the repository administrator via email ([scholarship@uwindsor.ca](mailto:scholarship@uwindsor.ca)) or by telephone at 519-253-3000ext. 3208.

**HYPERVELOCITY IMPACT ON SATELLITE SANDWICH STRUCTURES:  
DEVELOPMENT OF A SIMULATION MODEL AND INVESTIGATION OF  
PROJECTILE SHAPE AND HONEYCOMB CORE EFFECTS**

By

**Reihaneh Aslebagh**

A Thesis  
Submitted to the Faculty of Graduate Studies  
through the Department of Mechanical, Automotive and Materials Engineering  
in Partial Fulfillment of the Requirements for  
the Degree of Master of Applied Science  
at the University of Windsor

Windsor, Ontario, Canada

2021

© 2021 Reihaneh Aslebagh

**HYPERVELOCITY IMPACT ON SATELLITE SANDWICH STRUCTURES:  
DEVELOPMENT OF A SIMULATION MODEL AND INVESTIGATION OF  
PROJECTILE SHAPE AND HONEYCOMB CORE EFFECTS**

by

**Reihaneh Aslebagh**

APPROVED BY:

---

N. Van Engelen

Department of Civil and Environmental Engineering

---

V. Stoilov

Department of Mechanical, Automotive & Materials Engineering

---

A. Cherniaev, Advisor

Department of Mechanical, Automotive & Materials Engineering

March 24, 2021

## DECLARATION OF CO-AUTHORSHIP / PREVIOUS PUBLICATION

### I. Co-Authorship

I hereby declare that this thesis incorporates material that is result of my research in hypervelocity impact on satellite sandwich structures under the supervision of Dr. Aleksandr Cherniaev and his particular contributions in terms of supervision, project administration and funding acquisition.

I am aware of the University of Windsor Senate Policy on Authorship and I certify that I have properly acknowledged the contribution of other researcher to my thesis, and have obtained written permission from the co-author to include the above material(s) in my thesis.

I certify that, with the above qualification, this thesis, and the research to which it refers, is the product of my own work.

### II. Previous Publication

This thesis includes one original paper that has been previously submitted for publication in peer reviewed journals, as follows:

Thesis Chapter	Publication title/ full citation	Publication status
Chapter 3 and 4	“Development Of A Simulation Model And Investigation Of Projectile Shape And Honeycomb Core Effects”	Submitted

I certify that I have obtained a written permission from the copyright owner(s) to include the above material that has been submitted for publication in my thesis. I certify that the above material describes work completed during my registration as a graduate student at the University of Windsor.

### III. General

I declare that, to the best of my knowledge, my thesis does not infringe upon anyone's copyright nor violate any proprietary rights and that any ideas, techniques, quotations, or any other material from the work of other people included in my thesis, published or otherwise, are fully acknowledged in accordance with the standard referencing practices. Furthermore, to the extent that I have included copyrighted material that surpasses the bounds of fair dealing within the meaning of the Canada Copyright Act, I certify that I have obtained a written permission from the copyright owner(s) to include such material(s) in my thesis.

I declare that this is a true copy of my thesis, including any final revisions, as approved by my thesis committee and the Graduate Studies office, and that this thesis has not been submitted for a higher degree to any other University or Institution.

## ABSTRACT

Numerous Earth observations, communications, and scientific satellites have been developed in Canada or with significant Canadian participation over the last few decades, and many are currently being developed. To ensure mission success goals, space satellites in Earth orbit must be analyzed for their ability to survive hypervelocity impacts (HVI) by orbital debris, as collision of a functional satellite with even a millimeter-sized object traveling at typical orbital speed (7 km/s and higher) that can be detrimental for the Earth's orbit environment generating new orbital debris which may damage other spacecraft.

These collisions can also result in damage of components vital for satellite functioning (e.g., electronics units or connecting cables) or bursting of pressurized containers, such as satellite propellant tanks. In a typical unmanned satellite, this impact-sensitive equipment is usually situated in the enclosure of the **honeycomb-core sandwich panels**. These panels form the satellite's shape and are primarily designed to resist launching loads and provide attachment points for satellite subsystems. With low additional weight penalties, their intrinsic ballistic performance can often be upgraded to the level required for orbital debris protection.

This study aims to develop and validate simulation models for HVI on honeycomb-core sandwich panels to enable accurate assessment of orbital debris impact survivability of space satellites. The developed and validated model will be then used to conduct parametric studies and investigate different impact conditions (spherical vs. non-spherical projectile impacts), and effects of panel design parameters, such as honeycomb core cell size and foil (wall) thickness, on ballistic performance of sandwich panels.

## DEDICATION

This thesis is dedicated to my parents, my siblings, and my brother-in-law.

## ACKNOWLEDGEMENTS

First, I would like to truly thank my supervisor Dr. Aleksandr Cherniaev for giving me the excellent opportunity to pursue my master's research program with him. It has been a great pleasure for me to work under his supervision and I will be thankful to him forever. He has been a wonderful teacher for me and his professional lessons will stay as precious assets throughout my life.

My gratitude goes to my committee members, Dr. Stoilov and Dr. Van Engelen, for their valuable comments and guidance.

Last and most importantly, I would like to thank my family. I am so much blessed to have wonderful parents who have given me the love and support that has been inspiring me every day of my life. I want to thank my encouraging sisters and brother-in-law who have been by my side throughout my life.



## TABLE OF CONTENTS

DECLARATION OF CO-AUTHORSHIP / PREVIOUS PUBLICATION .....	iii
ABSTRACT.....	v
ACKNOWLEDGEMENTS .....	vii
LIST OF TABLES .....	x
LIST OF FIGURES .....	xi
LIST OF ABBREVIATIONS/SYMBOLS.....	xiii
NOMENCLATURE .....	xiv
1: INTRODUCTION AND LITERATURE REVIEW .....	1
1.1 Introduction .....	1
1.2 Literature review .....	2
1.2.1 Shielding structures of unmanned spacecraft .....	2
1.2.2 The effect of projectile geometry on hypervelocity ballistic performance of spacecraft shielding structures .....	7
1.2.3 The effect of honeycomb parameters on hypervelocity ballistic performance of sandwich panels .....	10
1.3 Summary of chapter 1 .....	12
2: DEVELOPMENT OF THE SIMULATION MODEL .....	14
2.1 Hydrocode simulations.....	14
2.2 Material modeling .....	19
2.2.1 General notes .....	19
2.2.2 Equation of state .....	20
2.2.3 Strength model.....	22
2.3 Numerical model .....	26
2.4 Summary of Chapter 2 .....	33

3: RESULTS AND DISCUSSION.....	35
3.1 Validation of the simulation model.....	35
3.2 Projectile shape effects.....	41
3.3 Honeycomb core effects.....	47
3.4 Summary of Chapter 3 .....	52
4: CONCLUSIONS AND FUTURE WORK.....	53
4.1 Conclusions .....	53
4.2 Future work .....	54
APPENDIX.....	56
REFERENCES .....	71
VITA AUCTORIS .....	77

## LIST OF TABLES

Table 1 – Composition of Al2017-T4 and Al2024-T3 alloys.....	22
Table 2 – Material model parameters used to represent Al2017-T4 and Al6061-T6 in simulations .....	24
Table 3 – Predictions of the developed simulation model, compared with the available experimental and analytical data .....	37
Table 4 – Parameters of the projectiles used in this study .....	42
Table 5 – Test matrix and outcomes of the numerical experiments .....	44

## LIST OF FIGURES

Figure 1 – Space debris in low Earth orbit (Image: Ref. [2]) .....	1
Figure 2 – Fragmentation of a sub-centimeter particle colliding with a thin target at 7 km/s [4] .....	2
Figure 3 – Schematics of different spacecraft shields: a) Whipple shield; b) stuffed Whipple; c) honeycomb-core sandwich panel; d) foam-core sandwich panel [7]....	3
Figure 4 – Impact of a 7 km/s projectile on (a) a Whipple shield (experiment), and (b) a honeycomb-core sandwich panel (simulation) [7] .....	6
Figure 5 – An estimate obtained using Equation (4) for a spherical Al2024 projectile mass required to perforate a 2” honeycomb-core panel with Al6061-T6 face-sheets, as a function of honeycomb cell size (normal 7 km/s impact).....	11
Figure 6 – Cell size parameters for the equation (6).....	12
Figure 7 – Simulation of perforation using FEM and SPH [4] .....	14
Figure 8 – Approximation of field variables at a point using SPH method (left – 1D; right – 2D) [4] .....	15
Figure 9 – Conservation equations .....	16
Figure 10 – Computational cycle of SPH solver [4].....	18
Figure 11 – Percentage of solid and molten fragments in the debris cloud as a function of impact speed (aluminum-aluminum impacts) .....	21
Figure 12 – Temperature rise, as predicted by the Johnson-Cook model in simulations with shell and solid elements at two different impact velocities .....	25
Figure 13 – Isometric view of the developed HVI simulation model.....	26
Figure 14 – Top view of the developed simulation model .....	27
Figure 15 – Front view of the developed simulation model .....	27
Figure 16 – Rear view of the developed simulation model .....	28
Figure 17 – Schematic picture of NODES_TO_SURFACE contact.....	29
Figure 18 – An explicit representation of a honeycomb core using shell elements (visualization shows the “assigned” thickness of the shell elements) .....	30
Figure 19 – Comparison of different honeycomb cell sizes used in this study .....	31
Figure 20 – Structure of the developed simulation model for HVI on HCSP .....	32

Figure 21 – Predicted shape of the fragment cloud in case of 6.91 km/s collision of a 2.5 mm Al2017-T4 projectile with 1.3 mm-thick Al6061-T6 plate: (a) honeycomb is lacking; and (b) honeycomb is present .....	35
Figure 22 – Channeling of hypervelocity fragments by honeycomb cells (sectioned view) .....	36
Figure 23 – Front wall damage: simulation (red grid cell is 1×1 mm) vs. NASA experiment (HITF 9005, [61]) .....	38
Figure 24 – Honeycomb damage: simulation vs. NASA experiment (HITF 9005, [61]).....	38
Figure 25 – Rear wall damage: simulation (red grid cell is 1×1 mm) vs. NASA experiment (HITF 9005, [61]) .....	38
Figure 26 – Predicted rear facesheet damage as a function of projectile diameter.	40
Figure 27 – Equal-volume sphere, disk and ring projectiles .....	42
Figure 28 – Projectile-honeycomb cell alignment .....	43
Figure 29 – Effects of projectile shape and aspect ratio on damage to the rear facesheet (all projectiles have the same volume of 0.9 mm <sup>3</sup> ).....	46
Figure 30 – Ballistic limit of the HCSP in case of the ring projectile impact (AR = 3.0) .....	47
Figure 31 – Effect of honeycomb cell size on rear facesheet damage (all projectiles have the same aspect ratio of 3.0 and volume of 0.9 mm <sup>3</sup> ) .....	48
Figure 32 – Cell size and projectile/honeycomb alignment effect on fragment cloud expansion .....	49
Figure 33 – Foil thickness effect on fragment cloud expansion and damage to the rear wall .....	51

## LIST OF ABBREVIATIONS/SYMBOLS

AR	Aspect Ratio
BLE	Ballistic Limit Equation
EOS	Equation of State
FEM	Finite Element Method
FC	Foam Core
FW	Front Wall
HC	Honeycomb Core
HCSP	Honeycomb Sandwich Panel
SPH	Smoothed Particle Hydrodynamics
HVI	Hypervelocity Impact
HITF	Hypervelocity Impact Technology Facility
MPP	Massively Parallel Processing
NASA	National Aeronautics and Space Administration
RW	Rear Wall
SP	Sandwich Panel
SRL	Schäfer – Ryan – Lambert
WS	Whipple Shield

## NOMENCLATURE

A	Initial yield strength in the Johnson-Cook strength model
a	Unitless, first order volume correction to $\gamma_0$
B	Hardening constant in the Johnson-Cook strength model
C	Strain rate constant in the Johnson-Cook strength model
C	Intercept of the $v_s = f(v_p)$ curve
$D_{\text{cell}}$	Honeycomb cell diameter
$d_c, D_{\text{cr}}$	Critical projectile diameter
E	Internal energy
G	Shear modulus
h	Smoothing length in weighing kernel function
J	Second deviatoric stress tensor constant
$K_{3D}$	BLE fit factor
m	Thermal softening exponent in Johnson-Cook strength model
$m_{\text{shield}}$	Overall shield areal density
$m_{\text{Nextel-Kevlar}}$	Nextel and Kevlar areal density
n	Hardening exponent in the Johnson-Cook strength model
p	Hydrostatic pressure
q	Cell size
2r	Cell pitch
S	Standoff distance
$S_1, S_2, S_3$	Unitless coefficient
$S^{\alpha\beta}$	Deviatoric stress tensor
$T_H$	Homologous temperature
$t_{\text{HC}}$	Honeycomb core thickness
$t_w, t_{\text{RW}}$	Rear wall thickness
V, $v_p$	Projectile velocity
$W_{ij}$	Weighting kernel function
Y	Flow stress
$\rho_w$	Rear wall density

$\rho_{FW}$	Front facesheet (“front wall”) density
$\rho_p$	projectile density
$\rho_b$	Bumper density
$\theta$	Impact angle from target normal
$\gamma_0$	Unitless Gruneisen gamma
$\mu$	Measure of compression (or expansion)
$\delta^{\alpha\beta}$	Kronecker delta
$\sigma$	Yield stress
$\sigma_{Y,FW}$	Yield stress of the front facesheet material
$\sigma'$	Stress deviatoric tensor
$\sigma^{\alpha\beta}$	Full stress tensor
$\epsilon_p$	Effective plastic strain
$\dot{\epsilon}_p^*$	Normalized effective plastic strain rate
$\dot{\epsilon}^{\alpha\beta}$	Strain rate tensor



# 1: INTRODUCTION AND LITERATURE REVIEW

## 1.1 Introduction

The growth of human activity in space led over the years to the formation of a significant number of unusable man-made objects circling Earth. These objects are known as “space junk” or “orbital debris” as shown in Figure 1 and characterize dysfunctional spacecraft, mission-related debris, and fragmentation debris generated by collisions and explosions in Orbit. According to NASA [1], the current population of orbital debris consists of more than 21,000 unemployed objects with a size larger than 100 mm; about 500,000 objects between 10 and 100 mm; and over 100,000,000 debris particles smaller than 10 mm.

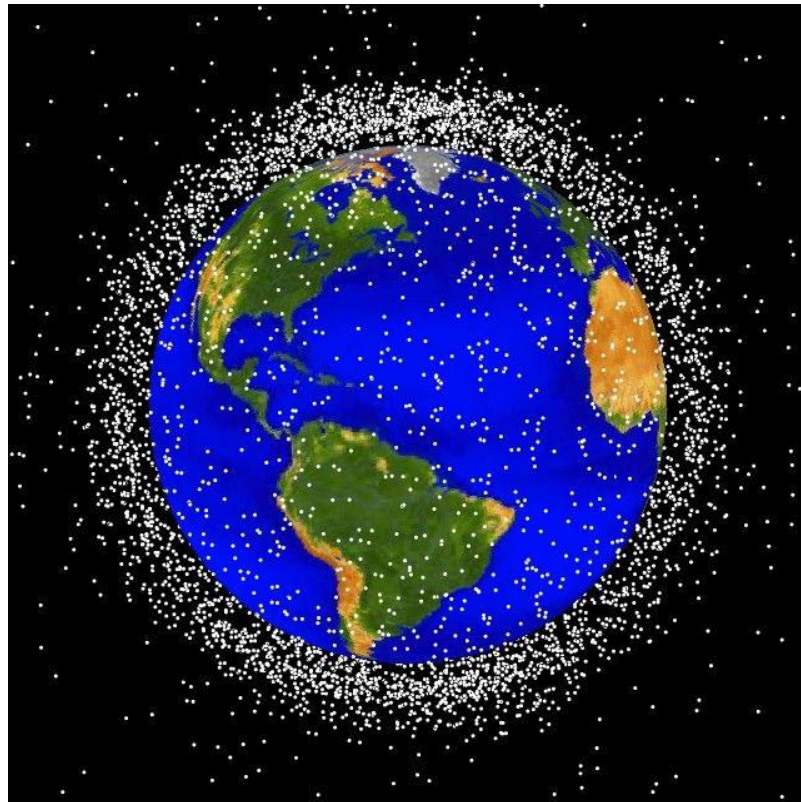


Figure 1 – Space debris in low Earth orbit (Image: Ref. [2])

Collisions with orbital debris happen at orbital speeds, usually exceeding 7 km/s, which corresponds to the hypervelocity impact (HVI) regime, when the impact speed is higher than the speed of sound in the colliding materials. A characteristic feature of HVI

is the fragmentation of the projectile and the target in the region of impact, which is caused by very high pressures, usually exceeding the strength of the colliding materials by orders of magnitude [3]. This scenario is exemplified in Figure 2 (left – just before collision; right – expanding fragment cloud after perforation of the front wall).

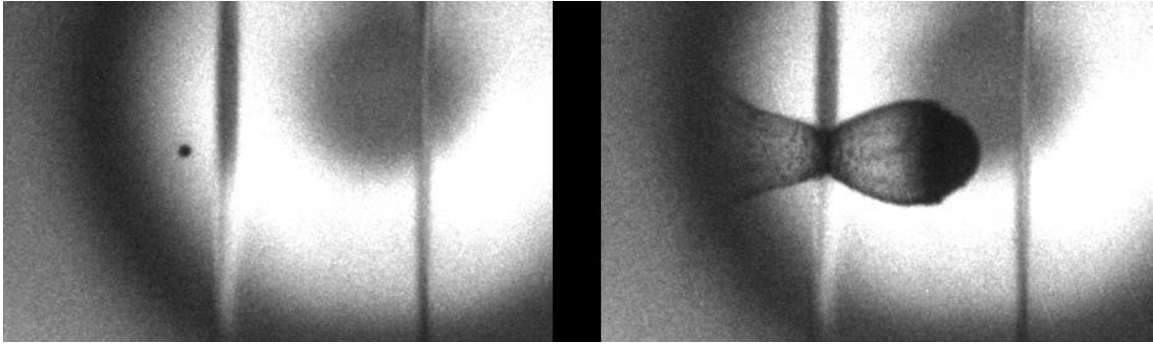


Figure 2 – Fragmentation of a sub-centimeter particle colliding with a thin target at 7 km/s [4]

To ensure mission success, satellites must be analyzed for their ability to survive HVI by orbital debris, described as collision of a functional satellite with even a millimeter-sized object traveling at distinctive orbital speed can be harmful to both the spacecraft and the Earth's orbital environment [5]. Consequences of these impacts may include loss-of-spacecraft failures owing to damage of components vital for the satellite operation (e.g., electronics units or connecting cables), as well as the explosion of pressurized containers such as satellite propellant tanks. In turn, this can cause multibillion-dollar financial losses for spacecraft owners and have a significant negative impact on the Earth's orbital environment due to the generation of new orbital debris. To avoid such scenarios, adequate shielding of the spacecraft against orbital debris must be ensured [6].

## 1.2 Literature review

### 1.2.1 Shielding structures of unmanned spacecraft

Spacecraft protective systems usually include spaced thin sheets (metallic or composite), such that the first sheet fragments a hypervelocity projectile, while the other layers provide additional fragmentation and/or collect the fragments (same as the rear wall

in Figure 2). Configurations of several commonly used spacecraft shielding systems are schematically illustrated in Figure 3.

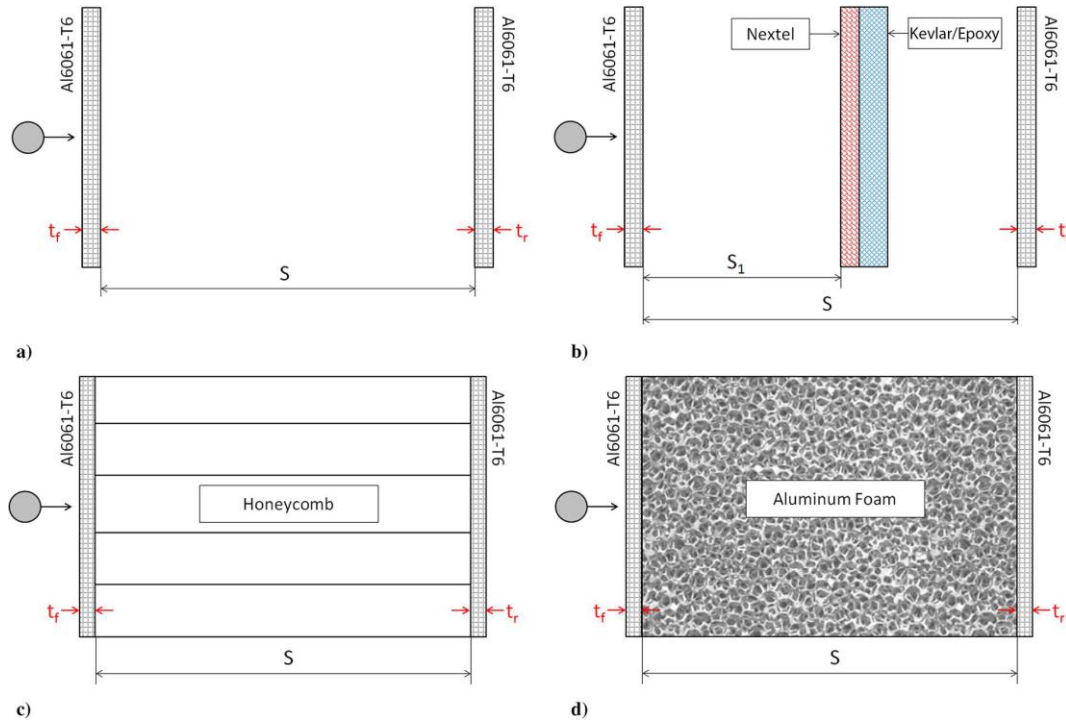


Figure 3 – Schematics of different spacecraft shields: a) Whipple shield; b) stuffed Whipple; c) honeycomb-core sandwich panel; d) foam-core sandwich panel [7]

### Single-purpose shields

Efforts to design lightweight orbital debris shields have been mainly driven by the need to protect habitable modules of the International Space Station (e.g., [8, 9, 10, 11]), which were designed as pressurized thin-walled structures with limited ability to absorb and dissipate the energy of hypervelocity projectiles. Accordingly, they are equipped with single-purpose shielding. Protective properties of such single-purpose shields as the Whipple shield, [12, 13], stuffed Whipple [14, 15], and multiwall shield [13] were extensively investigated.

Based on these studies, manufacturers have developed and adopted so-called ballistic limit equations (BLEs) – empirical response-surface models linking critical projectile diameter that can cause shield perforation with the impact conditions (projectile speed and material) and shield design parameters [15, 3, 16, 17]. Whipple shield and

Nextel/Kevlar Stuffed Whipple Shield BLEs are provided in Equations (1) and (2) respectively.

$$d_c = 3.918 t_w^{2/3} \rho_p^{-1/3} \rho_b^{-1/9} (V \cos \theta)^{-2/3} S^{1/3} (\sigma/70)^{1/3} \quad (1)$$

where

- $d_c$  is the critical projectile diameter at shield failure threshold [cm];
- $t_w$  is the rear wall thickness [cm];
- $\rho_p$  is the projectile density [g/cm<sup>3</sup>];
- $\rho_b$  is the bumper (facesheets) density [g/cm<sup>3</sup>];
- $V$  is the projectile velocity [km/s];
- $S$  is the standoff distance from the back of the bumper to the front of the rear wall [cm];
- $\theta$  is the impact angle from target normal [deg]; (note: impact at  $\theta = 0$  deg is normal to the target);
- $\sigma$  is the rear wall yield stress [ksi];

and

$$d_c = K_{H-SW} (t_w \rho_w)^{1/3} \rho_p^{-1/3} (\sigma/40)^{1/6} V^{-1/3} (\cos \theta)^{-0.5} S^{2/3} \quad (2)$$

where

- $d_c$  is the critical projectile diameter at shield failure threshold [cm];
- $K_{H-SW} = 0.6 [\text{km}^{1/3} \text{S}^{-1/3}]$  when  $m_{\text{Nextel-Kevlar}} = 0.25 m_{\text{shield}}$  to  $0.35 m_{\text{shield}}$
- $K_{H-SW} = 0.45 [\text{km}^{1/3} \text{S}^{-1/3}]$  when  $m_{\text{Nextel-Kevlar}} = 0.1 m_{\text{shield}}$  to  $0.15 m_{\text{shield}}$
- $m_{\text{Nextel-Kevlar}}$  = Nextel and Kevlar areal density [g/cm<sup>2</sup>]
- $m_{\text{shield}}$  = overall shield areal density [g/cm<sup>2</sup>]
- $m_{\text{shield}} = m_{\text{bumper}} + m_{\text{Nextel-Kevlar}} + m_{\text{rear-wall}}$
- $t_w$  is the rear wall thickness [cm];
- $\rho_w$  is the rear wall density [g/cm<sup>3</sup>];
- $\rho_p$  is the projectile density [g/cm<sup>3</sup>];
- $\sigma$  is the rear wall yield stress [ksi];

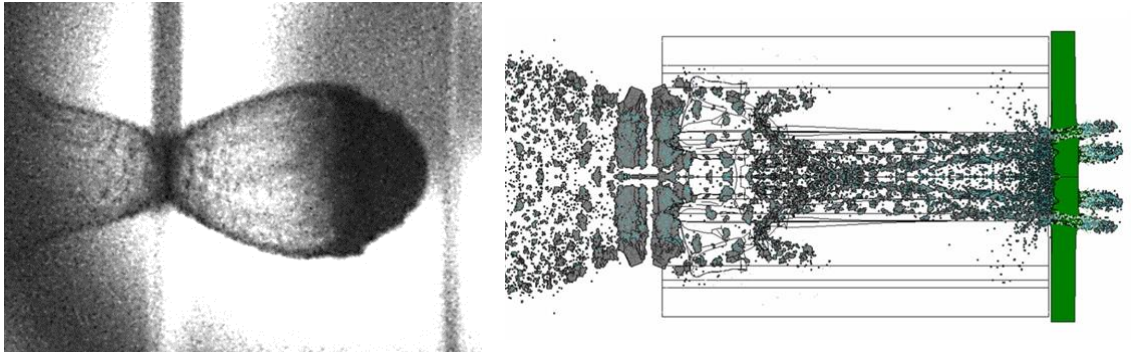
- $V$  is the projectile velocity [km/s];
- $\theta$  is the impact angle from target normal [deg]; (note: impact at  $\theta = 0$  deg is normal to the target)
- $S$  is the overall spacing (gap distance) between the outer bumper and the rear wall [cm].

### Multi-purpose shields

Structures of unmanned (robotic) satellites are usually different from manned spacecraft, and it is often possible to use multifunctional design strategies for greater weight efficiency instead of the single-purpose shielding [18]. In a typical satellite bus design (e.g., Canadian CASSIOPEE and RADARSAT satellites), most impact-sensitive equipment is situated in the enclosure of the structural sandwich panels. Being the most commonly used elements of satellite structures, these panels form the satellite's shape and are primarily designed to resist launching loads and provide attachment points for satellite subsystems [19]. With low additional weight penalties, their intrinsic ballistic performance can often be upgraded to the level required for orbital debris protection [7, 20, 21]. On the other hand, perforation of a structural panel sends high-speed debris into the satellite and can be considered as a failure criterion for most otherwise unprotected components (e.g., circuit boards, cables, etc.) and components that are highly vulnerable to orbital debris impacts (e.g. pressurized propellant tanks). Consequently, assessing the orbital debris impact survivability of robotic satellites requires the availability of predictive models for sandwich panels capable of accounting for various impact conditions and design parameters.

Recent studies have aimed to characterize and compare the protective performance of two major types of sandwich panels (SP) used in spacecraft design: honeycomb-core (HC) and open-cell foam-core (FC) panels [22, 23; 10, 24]. Comparative evaluations conducted by researchers (e.g., [7], [25]), have revealed the superiority of open-cell foam-core panels for ballistic protection. In HCSP, honeycomb cells constrain expansion of the cloud of high-speed projectile fragments (projectiles are fragmented as a result of interacting with the panel's front face sheet) and focus fragments' impact energy and momentum on a small area on the rear face sheet, which adversely affects the panel's ballistic limit (so-called "channeling effect" of honeycomb; e.g., [26, 27]). This channeling

effect is illustrated in Fig. 4 (b) in comparison with the unconstrained fragment cloud resulting from HVI on a Whipple shield (Fig. 4 (a)). Conversely, the projectile fragments' interaction with individual ligaments of an open-cell foam was found to result in significantly reducing the fragments' damaging potential (so-called “multishock effect” of foam; e.g., [10, 24]). However, owing to the multiplicity of possible requirements for multifunctional panels, it can be expected that both HC and FC structures will find applications in future satellite design.



(a) Dual wall (Whipple) shield

(b) Honeycomb core sandwich panel

Figure 4 – Impact of a 7 km/s projectile on (a) a Whipple shield (experiment), and (b) a honeycomb-core sandwich panel (simulation) [7]

Several studies have been dedicated to developing BLEs for honeycomb-core sandwich panels [27, 28, 29]. In all of such studies, ballistic limit equations represented modifications of the BLE for double-wall Whipple shield (two separated thin sheets without intermediate core material). Comparison of HCSP BLEs is provided in [28]. Even most successful among them features limited goodness of fit, as outcomes of only about 70% of experiments initially used for the BLE calibration could be then correctly predicted by it. This BLE is provided in Equation (3) (named after its developers: Schaefer-Ryan-Lambert, SRL BLE).

$$d_c = \frac{1.155 \cdot S^{1/3} \cdot t_w^{2/3} \cdot \left(\frac{\sigma_y}{70}\right)^{1/3}}{K_{3D}^{2/3} \rho_p^{1/3} \rho_b^{1/9} V^{2/3} (\cos\theta)^\delta} \quad (3)$$

Here

- $d_c$  is the critical projectile diameter [cm];
- $S$  is the spacing between the facesheets (honeycomb core thickness) [cm];
- $t_w$  is the rear wall thickness [cm];
- $K_{3D}$  is the BLE fit factor, which is equal to 0.4 in the case of aluminum-on-aluminum impacts
- $\rho_p$  is the projectile density [ $\text{g}/\text{cm}^3$ ];
- $\rho_b$  is the bumper (front facesheet) density [ $\text{g}/\text{cm}^3$ ];
- $V$  is the projectile velocity [km/s];
- $\sigma_y$  is the yield stress of the front facesheet material [ksi].

### 1.2.2 The effect of projectile geometry on hypervelocity ballistic performance of spacecraft shielding structures

Most of the existing BLEs have been developed based on the hypervelocity impact experiments conducted with spherical projectiles; however, orbital debris geometry is not constrained to spherical shape and may be significantly different. Researchers conducted experiments (less often due to their expensiveness) and/or employed numerical simulations and modeling (more often) in order to investigate these more sophisticated impact scenarios involving different projectile geometries. The summary of the findings of these studies is provided below.

#### Elliptical projectiles

Carrasquilla and Miller used experimental results obtained at the Ernst-Mach Institute, in which rotationally symmetric ellipsoids were used as the impactors, to analyze validity of the conventional Whipple shield BLE for these projectile shapes. The projectile's shape effect was considered by changing just one parameter, namely the shape factor,  $f$ . It was defined as the ratio of the length of the projectile to its diameter (e.g., the shape factors of 1,  $< 1$ , and  $> 1$  would characterize a sphere, an oblate ellipsoid, and a prolate ellipsoid, respectively). It was concluded that BLE for spheres reasonably predict failure of a Whipple shield at low impact velocities, but need to be adjusted for hypervelocity regime (velocities above 4 km/s) [30].

Schaefer et al. proposed a modification of the Cour-Palais thick target penetration formula [13] to account for projectile shape effects by including in it the abovementioned shape factor. Their test and simulation results confirmed that the projectile shape influences severely the penetration depth in a semi-infinite target [31].

#### Conical projectiles

Liu et al. investigated the effect of the conical projectiles with different length-to-diameter ratios ( $L/D$ ) and impact orientations on the ballistic performance of the spacecraft shields using the implementation of the smoothed particle hydrodynamics (SPH) method in AUTODYN software [32]. Their findings indicated that different  $L/D$  ratios and cone orientations result in a considerable change in the debris cloud shape, such that the clouds become significantly more focused with the increase of the ratio. This can be an indication of increasing “lethality” of the fragment cloud with elongation of the projectiles.

#### Cubical projectiles

Vignjevic et al. found that in the hypervelocity regime, the debris cloud produced by a cubical projectile has the highest normalized axial velocity, as compared with that of spherical and cylindrical projectile [33].

Based on their numerical study, Silnikov et al. deduced that the characteristics of the debris cloud in a “face-on” impact with cubical projectiles are different as compared with the “edge-on” impact. In particular, the fragments spread over a larger area between the bumper and the rear wall in face-on impact. However, the cloud is denser after edge-on impact, and most of the initial mass of the projectile is focused on the impact axis. It can, therefore, be more penetrating to the rear wall of the Whipple shield [34].

#### Cylinders ( $L/D > 1$ ) and disks ( $L/D < 1$ )

Morrison et al. experimentally investigated the ballistic performance of a dual-wall Whipple shield in case of impacts of equal-mass spherical and cylindrical projectiles (different  $L/D$  ratios) with velocities near 7 km/sec. It was found that when only bulging and no perforation of the rear wall was observed in the case of spherical projectile, it was fully perforated by the cylinders. Higher  $L/D$  ratios (above unity) led to increased



concentration of the fragments and increase of hole diameter in the rear wall. In contrast, the L/D ratio of 1 resulted in minimal damage to the rear wall. Preventing perforation in the rear wall required a reduction in mass of the cylinder to a value much less than that of the sphere to avoid the penetration of the structure [35].

This was supported by Piekutowski, who demonstrated that the L/D ratio of cylindrical projectiles has a significant influence on the debris cloud ability to perforate the rear wall of the spacecraft's shield and also concluded that with the same impact velocity, the mass of cylindrical projectile that fully perforates a shield is less than of the spherical projectile. Disks striking the wall of a Whipple shield with their axis coinciding with the impact axis in a normal impact create fragments cloud not spreading widely (a “column-shaped” fragment cloud). Therefore, they can be very damaging and penetrative to the rear wall [36].

Christiansen et al. conducted a study involving spherical and hollow cylindrical (thick-walled pipe) projectiles with the L/D ratio ranging from 1 to 3 for the latter. The considered shield structures were the regular and the stuffed Whipple shield. The authors concluded that a sphere with the same mass as the hollow cylinder projectile is less damaging [14].

Hu and Schonberg carried out a series of 2D axisymmetrical simulations comparing penetrating capability of spherical and cylindrical projectiles with L/D ratios ranging from 0.2 (“disk”) to 5.0 (“long cylinder”) [37]. The sphere was found to be the least dangerous shape compared with the other considered projectiles. For impact velocities over 7.5 km/s, the longest cylinders and flattest (= “longest”) disks demonstrated highest perforating ability. This conclusion was supported by Schonberg and Williamsen [38] in a numerical study, which, in addition to cylindrical and spherical projectiles, considered such shapes as cones and cubes. High perforating ability of flat geometries was also noted by Chhabildas et al. [39], who found that thin plates can be more damaging to the rear wall of the Whipple shield as compared to spherical projectiles at impact velocities of about 10 km/s.

Miller, in a recent study, conducted near six hundred simulations of 7 km/s disk-shaped composite projectile impacts, investigating the effect of the projectile orientation

on ballistic performance of aluminum Whipple shield with a thermal blanket. It has been found that the flat disk-like penetrators with high pitch, when the disk axis is orthogonal to the velocity vector, are of the highest concern [40].

### 1.2.3 The effect of honeycomb parameters on hypervelocity ballistic performance of sandwich panels

The SRL BLE [see Equation (3)] does not include any parameters characterizing the geometry of honeycomb cells.

However, Christiansen et al. [3] suggest evaluating the ballistic performance of HCSPs subjected to HVI using the Whipple shield BLE [see Equation (1)], in which the parameter  $S$ , representing the standoff distance in the original WS equation, is replaced by either the product of twice the honeycomb cell diameter ( $D_{\text{cell}}$ ) or by the core thickness ( $t_{\text{HC}}$ ), whichever is less:

$$S = \min(2D_{\text{cell}}; t_{\text{HC}}) \quad (4)$$

This constraint reflects the fact that honeycomb panels are more easily penetrated as compared to the dual walls, because of channeling of the debris cloud after perforation of the first face-sheet, and suggests that the size of honeycomb cell may have a significant effect on the panel's ballistic performance. They emphasize, however, this approach can only be used as a rough estimate. Simple calculations conducted using Equation (4) with different commercially available honeycomb cell sizes illustrate that a required projectile mass needed to perforate a 2" aluminum HCSP can vary significantly depending on the cell dimensions (see Figure 5).

This is in line with the findings of Kang et al. who through a series of numerical simulations, concluded that the HC core cell size is the most influential parameter on the damage of the rear face-sheet due to the channeling effect [41]. Same conclusions regarding the HC cell size effect have been made by Ilescu et al. in Ref. [42] and Schubert et al. in Ref. [43]. The latter concluded that cell size and foil thickness of the honeycomb core considerably influence HVI protective performance of HCSPs, but have not been properly accounted for yet in existing ballistic limit equations. Such HCSP-specific BLEs

that do not take into account the effect of honeycomb cell size on the ballistic performance of sandwich panels either completely or in certain conditions will be discussed below.

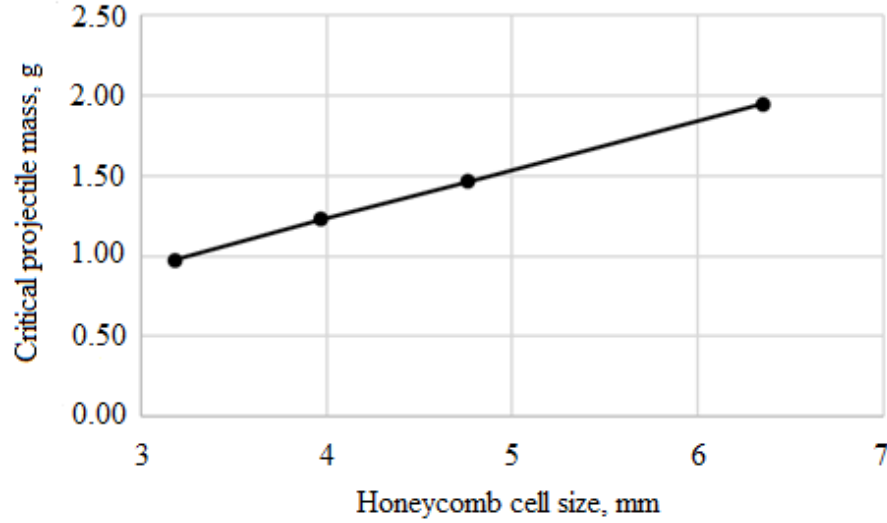


Figure 5 – An estimate obtained using Equation (4) for a spherical Al2024 projectile mass required to perforate a 2” honeycomb-core panel with Al6061-T6 face-sheets, as a function of honeycomb cell size (normal 7 km/s impact)

Sibaud et al. [23] derived the following BLE for calculating critical projectile diameter in case of HVI with  $v_p \geq 7$  km/s on HCSP:

$$d_c = \left[ \frac{0.286 \cdot (t_{HC} + t_{RW}) \sqrt{S}}{\left(\frac{\sigma}{70}\right) \rho_p^{0.5} V_p \cos \theta \rho_{FW}^{0.167}} \right]^{2/3} \quad (5)$$

where

- subscripts “FW” and “RW” refer to the front and rear face-sheet of the panel, respectively;
- $t_{HC}$  is the total thickness of honeycomb cell walls [cm];
- $\rho_p$  is the projectile density [g/cm<sup>3</sup>];
- $\rho_b$  is the bumper (facesheets) density [g/cm<sup>3</sup>];
- $V_p$  is the projectile velocity [km/s];
- $S$  is the spacing between the facesheets [cm];

- $\theta$  is the impact angle from target normal [deg]; (note: impact at  $\theta = 0$  deg is normal to the target)
- $\sigma$  is the rear wall yield stress [ksi].

It should be noted that, unlike Equation (4),  $t_{HC}$  in Equation (5) is the thickness of honeycomb cell walls which will be perforated by the projectile with incidence  $\theta$ :

$$t_{HC} = \left[ 0.014 \times r \times \text{Int} \left( \frac{S \times \tan \theta}{q} \right) \right]^{0.293} \quad (6)$$

where parameters  $q$  and  $r$  in Equation (6) characterize the geometry of the honeycomb cell, as shown in Figure 6. Importantly, parameter  $t_{HC}$  is a function of the impact obliquity and will be zero for normal impacts. Therefore, Equation (5) does not take into account the effect of honeycomb cell size in case of normal impact.

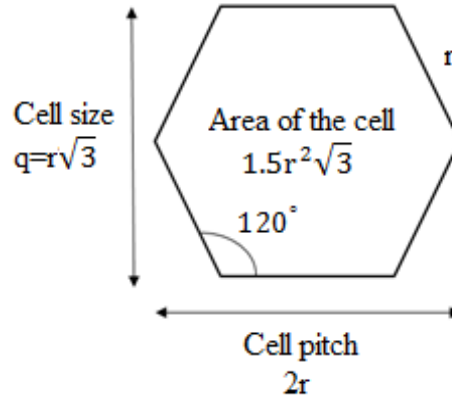


Figure 6 – Cell size parameters for the equation (6)

### 1.3 Summary of chapter 1

The following conclusions can be made based on the conducted literature review:

- Previous studies indicate that projectile shape can have a very significant effect on its penetrating ability in case of hypervelocity impact. While multiple projectile shapes have been studied, it can be concluded that long cylinders and **flat disks with high pitch angles** are among the most damaging shapes.
- The existing studies considered such protective structures as thick plates, Whipple, and stuffed Whipple shield, while there is a lack of investigations of projectile shape effect

on the ballistic performance of another commonly used class of shields – sandwich panels.

- Although it is generally recognized that the effect of honeycomb core cell size on HVI ballistic performance of HCSPs can be significant, it is not usually taken into account by the existing predictive models and requires additional investigation.

Correspondingly, in order to fill the gap in the existing knowledge, the objectives of this study were formulated as follows:

1. Develop and validate a high-fidelity simulation model for hypervelocity impact on spacecraft honeycomb-core sandwich panels.
2. Investigate the effect of high-pitch-angle disk-like projectile impacts on protective properties of spacecraft sandwich structures with honeycomb cores.
3. Investigate the effect of honeycomb cell size on the ballistic performance of HCSP subjected to impacts by high-pitch-angle disk-like projectiles.

## 2: DEVELOPMENT OF THE SIMULATION MODEL

### 2.1 Hydrocode simulations

The combined use of finite element method (FEM) in the Lagrangian formulation and smoothed particles hydrodynamics (SPH) – a meshless solver – is utilized in HVI simulations throughout this study (Fig. 7). As SPH is a relatively new technique, it will be described in more details in this section.

Although FEM, in general, provides a good balance between simulation accuracy and computational efficiency, it usually requires the use of a non-physical erosion algorithm to avoid mesh distortion and tangling at high deformation levels, and depends on the selected critical geometric strain that should be calibrated by comparison with experimental data and it is not known by default [44].

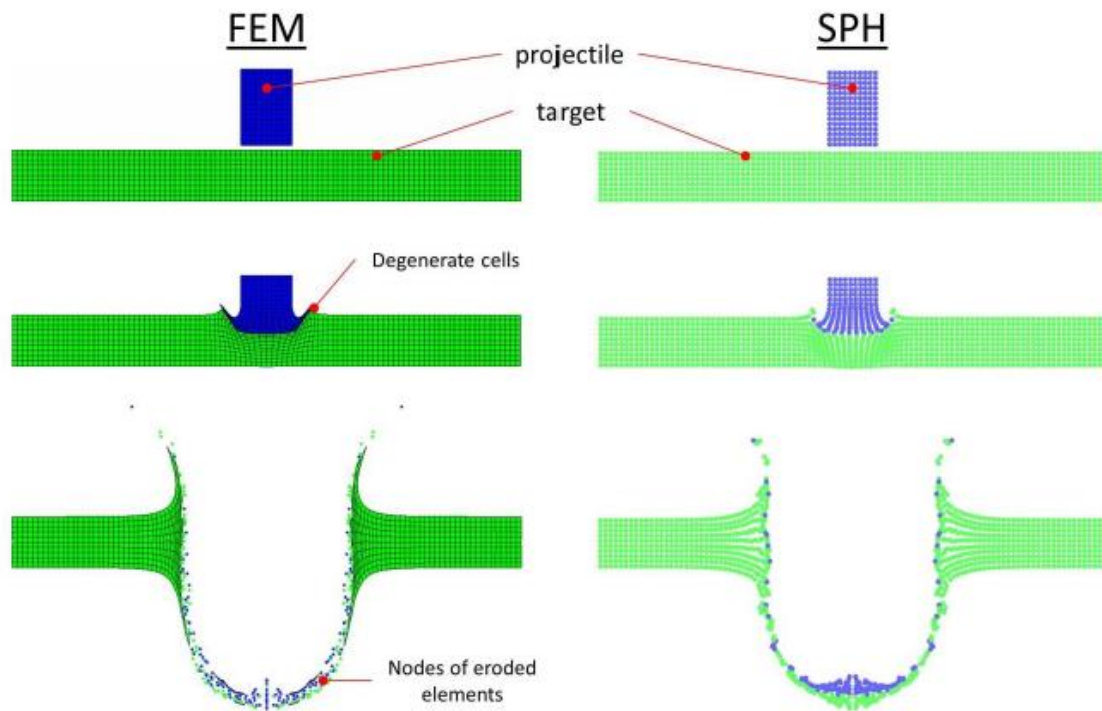


Figure 7 – Simulation of perforation using FEM and SPH [4]

SPH is a meshless Lagrangian method developed for numerically solving problems formulated in terms of partial differential equations of field variables, such as density,

velocity, energy, etc. Unlike FEM, SPH method utilizes “particles” for continuum discretization. The particles are not simple interacting mass points. Instead, they are used for interpolation in order to estimate values of the field variables and their derivatives in discrete points of continuum.

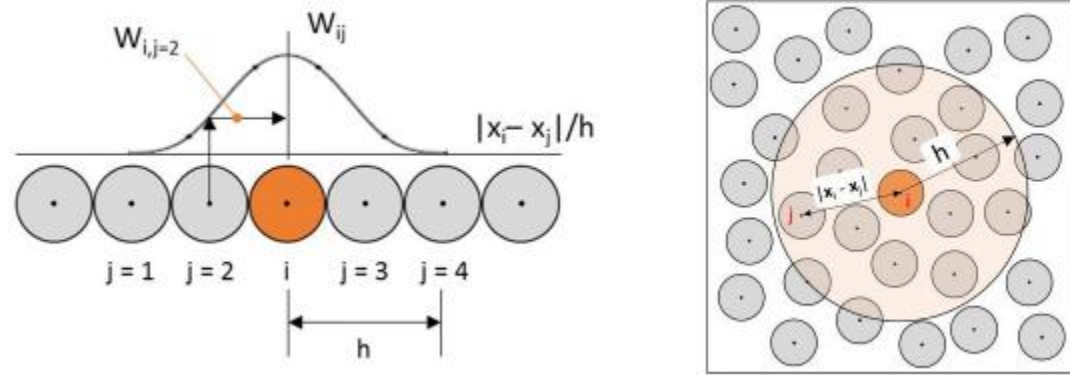


Figure 8 – Approximation of field variables at a point using SPH method (left – 1D; right – 2D) [4]

The interpolation uses a weighting function (often referred to as "kernel") to approximate the field variables and their derivatives at any point of the domain. Equation (7) demonstrates that the density at a point  $i$  with coordinates  $x_i$  can be estimated from the adjacent particles as

$$\rho_i = \sum_j m_j \cdot W_{ij}(|x_i - x_j|, h) \quad (7)$$

Where

- $m_j$  is the mass of  $j$ -th particle;
- $W_{ij}$  is a weighting kernel function (typically a cubic B-spline); and
- $h$  is so-called smoothing length, which determines a support domain for approximation, as it is exemplified in Fig. 8 for a one-dimensional and a two-dimensional case.

Another example can be given for the strain rate tensor  $\dot{\epsilon}^{\alpha\beta} = \frac{1}{2} \left( \frac{\partial v^\alpha}{\partial x^\beta} - \frac{\partial v^\beta}{\partial x^\alpha} \right)$  for which the SPH approximation can be written as follows [45]:

$$\dot{\epsilon}^{\alpha\beta} = \frac{1}{2} \sum_j \frac{m_j}{\rho_j} \left( (v_j^\alpha - v_i^\alpha) \frac{\partial W_{ij}}{\partial x_i^\beta} + (v_j^\beta - v_i^\beta) \frac{\partial W_{ij}}{\partial x_i^\alpha} \right) \quad (8)$$

Figure 9 demonstrates the conservation equations of continuum mechanics and their SPH approximations. The derivation of these approximations can be found in [46].

	Continuum mechanics	SPH approximation
Conservation of mass	$\frac{d\rho}{dt} = -\rho \cdot \frac{\partial v^\beta}{\partial x^\beta}$	$\frac{d\rho_i}{dt} = -\rho_i \sum_j \frac{m_j}{\rho_i} (v_i^\beta - v_j^\beta) \cdot W_{ij,\beta}$
Conservation of momentum	$\frac{dv^\alpha}{dt} = -\frac{1}{\rho} \cdot \frac{\partial \sigma^{\alpha\beta}}{\partial x^\beta}$	$\frac{dv_i^\alpha}{dt} = -\sum_j m_j \left( \frac{\sigma_i^{\alpha\beta}}{\rho_i^2} - \frac{\sigma_j^{\alpha\beta}}{\rho_j^2} \right) \cdot W_{ij,\beta}$
Conservation of energy	$\frac{de}{dt} = -\frac{\sigma^{\alpha\beta}}{\rho} \cdot \frac{\partial v^\alpha}{\partial x^\beta}$	$\frac{de_i}{dt} = -\frac{\sigma_i^{\alpha\beta}}{\rho_i^2} \sum_j m_j (v_i^\alpha - v_j^\alpha) \cdot W_{ij,\beta}$

Figure 9 – Conservation equations

In these equations,  $\sigma^{\alpha\beta}$  is the full stress tensor, which can be represented in terms of hydrostatic pressure  $p$  and deviatoric stress tensor  $S^{\alpha\beta}$ , as  $\sigma^{\alpha\beta} = p\delta^{\alpha\beta} + S^{\alpha\beta}$ . The hydrostatic pressure can be defined using an equation of state (EOS), such as Gruneisen EOS (see Section 2.2.2).

The fundamental equations that specify the components of the deviatoric stress tensor, can be formulated in different ways, depending on materials being used and physical behavior assumptions for a specific problem. For instance, in case of small displacements, it can be written as follows [46]:

$$\dot{S}^{\alpha\beta} = G \left( \dot{\epsilon}^{\alpha\beta} - \frac{1}{3} \delta^{\alpha\beta} \epsilon^{\gamma\gamma} \right) \quad (9)$$



where  $G$  is the shear modulus. For finite displacements, another expression can also be obtained for the frame independent stress rate including the rotation rate tensor, as can be found in [45] and [46].

The plastic flow regime can be determined by the Von-Mises criterion. When the second deviatoric stress tensor constant ( $J$ ) surpasses the flow stress ( $Y$ ), the individual deviators will be then brought back to the flow surface through the following adjustment:

$$S^{\alpha\beta} = S^{\alpha\beta} \sqrt{\frac{Y^2/3}{J^2}}. \quad (10)$$

The yield stress can be constant as the case of elasto-plastic material model or it can be a function of various parameters. For instance, the Johnson-Cook strength model applied to the modeling of metallic materials in this study, considers the influences of strain rate, strain hardening, and thermal softening on the flow stress (see section 2.2.3).

SPH is often more beneficial than FEM in physical simulations that undergo large deformations, high strain rates, fragmentation, and perforation owing to the lack of mesh tangling (since there is no mesh in SPH method) and no need to apply the artificial erosion mechanism. The SPH particles “naturally” create discontinuities in the continuum such as cracking, penetration, and fragmentation when particles are detached and fragmented during the penetration event. The principal drawback of SPH is tensile instability, i.e. numerical fractures may be generated in the high tensile stresses regions due to the lack of interaction between primarily adjacent particles [47,48].

The general computational cycle of SPH solver (at each timestep) is illustrated in Figure 10.

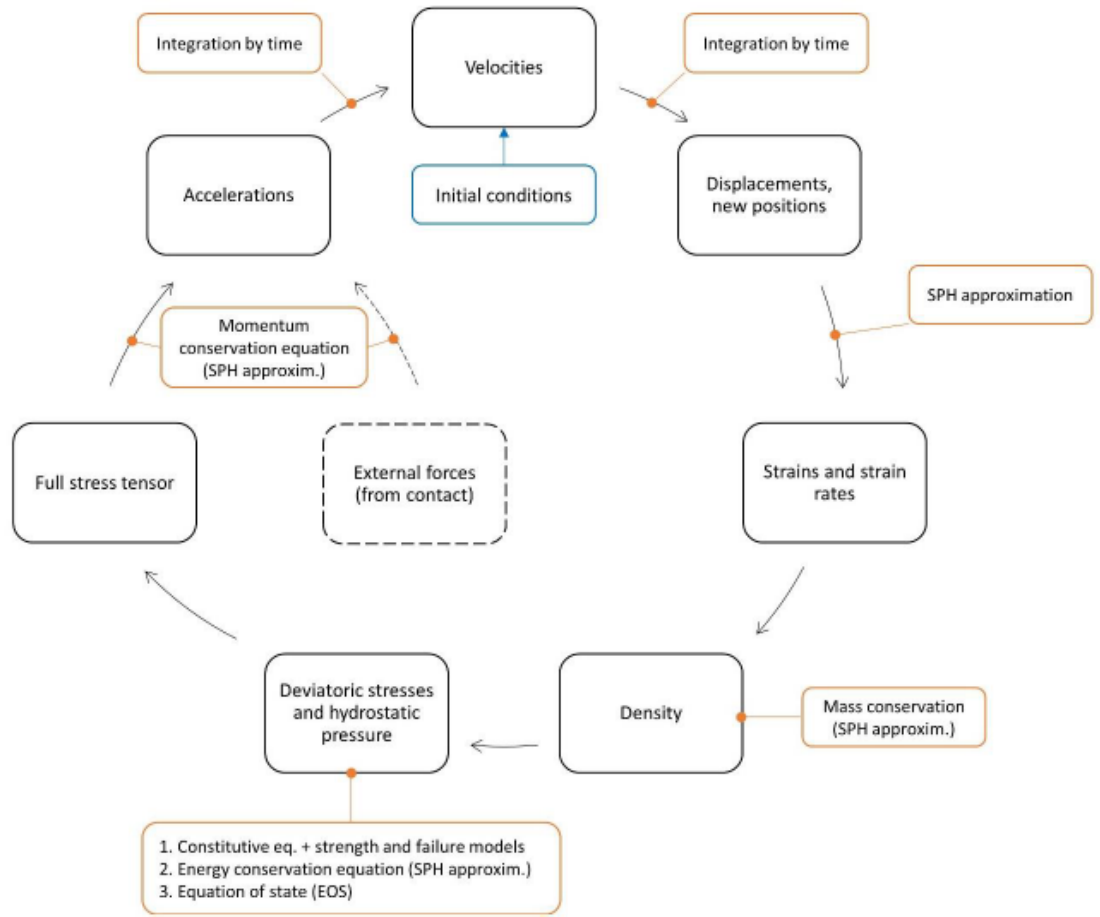


Figure 10 – Computational cycle of SPH solver [4]

Previous studies utilized both FEM and SPH methods in modeling of HVI scenarios. For example, Pezzica et al. [49] used Lagrangian finite elements to model hypervelocity impact of an aluminum sphere on a 3-walled aluminum structure. The nodes of eroded elements created the debris cloud in their simulation. For specific (adjusted) values of critical geometric strain, the results closely correlated with experimental data.

Other researchers successfully used SPH method in hypervelocity impacts simulations on different targets such as thin plate [50], stuffed Whipple shields [51], brittle targets [52], and laminated composite materials [53, 54].

## 2.2 Material modeling

### 2.2.1 General notes

Three distinct aluminum alloys, namely Al2017-T4, Al6061-T6, and Al5052-H34, were used in this study to represent the material of projectiles, HCSP facesheets, and honeycomb cores, respectively. This is consistent with the design of sandwich panels and projectiles used by NASA in their HVI experimental program, some of which were used in this study for validation of the numerical model.

A typical solid material model requires equations that relate stress to deformation and internal energy (or temperature). A stress tensor describes the “stress state” at a point in the body subjected to external loading:

$$\sigma = \begin{bmatrix} \sigma_{11} & \sigma_{12} & \sigma_{13} \\ \sigma_{21} & \sigma_{22} & \sigma_{23} \\ \sigma_{31} & \sigma_{32} & \sigma_{33} \end{bmatrix} \quad (11)$$

Here  $\sigma_{ii}$  – normal stresses, and  $\sigma_{ij}$  – shear stresses.

In most cases, the stress tensor may be separated into a uniform hydrostatic pressure (p):

$$p = -\frac{1}{3} \cdot (\sigma_{11} + \sigma_{22} + \sigma_{33}) \quad (12)$$

and a stress deviatoric tensor ( $\sigma'$ ) associated with the resistance of the material to shear distortion:

$$\sigma' = \begin{bmatrix} \sigma_{11} - p & \sigma_{12} & \sigma_{13} \\ \sigma_{21} & \sigma_{22} - p & \sigma_{23} \\ \sigma_{31} & \sigma_{32} & \sigma_{33} - p \end{bmatrix} \quad (13)$$

such that

$$\sigma = \sigma' - p \cdot \delta \quad (14)$$

Here  $\delta$  is a 3x3 identity (unit) matrix.

Correspondingly, pressure is calculated using an equation of state (EOS) and deviatoric stresses are computed using a strength model.

### 2.2.2 Equation of state

The relation between the hydrostatic pressure, the local density (or specific volume, or volumetric strain), and local specific energy (or temperature) is known as an equation of state. This relation can be obtained using the conservation equations (mass, momentum, and energy), which usually involves five unknowns:

1. pressure itself ( $p$ );
2. particle velocity ( $v_p$ );
3. shock velocity ( $v_s$ );
4. density ( $\rho$ ); and
5. energy ( $E$ ).

Therefore, in order to obtain the required relationship ( $p = f(\rho, E)$ ), an additional equation is needed. Typically, this additional equation is represented in terms of shock-velocity – particle-velocity relationship ( $v_s = f(v_p)$ ), as both of these quantities can be conveniently measured experimentally.

A widely used EOS for solid materials subjected to high-speed impact loading is the Gruneisen EOS [55], in which the  $v_s(v_p)$  relationship is assumed to be cubic:

$$v_s = C + S_1 v_p + S_2 v_p^2 + S_3 v_p^3 \quad (15)$$

The Gruneisen equation of state then defines pressure for compressed materials as

$$p = \frac{\rho_0 C^2 \mu \left[ 1 + \left( 1 - \frac{\gamma_0}{2} \right) \mu - \frac{a}{2} \mu^2 \right]}{\left[ 1 - (S_1 - 1) \mu - S_2 \frac{\mu^2}{\mu + 1} - S_3 \frac{\mu^3}{(\mu + 1)^2} \right]^2} + (\gamma_0 + a \mu) E \quad (16)$$

and for expanded materials as

$$p = \rho_0 C^2 \mu + (\gamma_0 + a \mu) E \quad (17)$$

Here

- $C$  is the intercept of the  $v_s = f(v_p)$  curve (in velocity units);
- $S_1, S_2$ , and  $S_3$  are the unitless coefficients of the slope of the  $v_s = f(v_p)$  curve;
- $\gamma_0$  is the unitless Gruneisen gamma;
- $a$  is the unitless, first order volume correction to  $\gamma_0$ ;
- $\mu$  is the measure of compression (or expansion),  $\mu = \frac{\rho}{\rho_0} - 1$ ;
- $E$  denotes the internal energy.

The Gruneisen EOS does not take into account phase changes that may happen with the material, however, a relatively small fraction of the fragment cloud usually undergoes phase transformations at 7 km/s impacts. An estimate based on information provided in Ref. [3] is shown in Fig. 11 for aluminum projectile-aluminum target impacts (vaporized fragments that are expected to appear in small quantities after 10 km/s are not accounted for in Fig. 11). As can be deduced from the figure, in the range between 6 and 7 km/s (the order of the orbital velocity), 85 – 95% of the cloud is represented by solid fragments, which justifies the use of Gruneisen EOS for that velocity range.

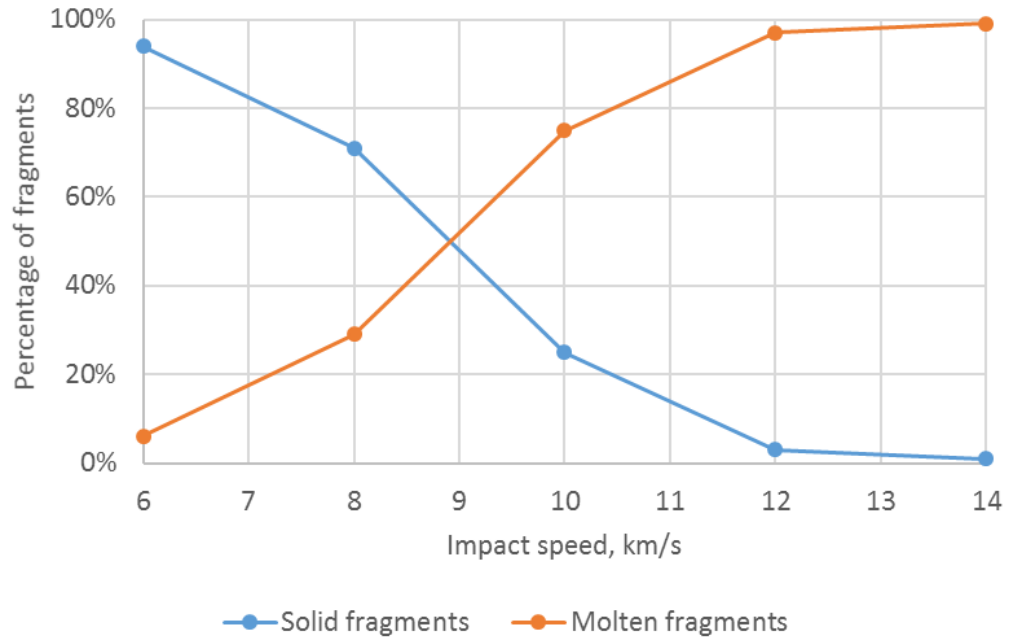


Figure 11 – Percentage of solid and molten fragments in the debris cloud as a function of impact speed (aluminum-aluminum impacts)

For many metals, including aluminum and its alloys, it has been observed that the  $v_s(v_p)$  relationship is linear [56], i.e.  $S_2 = S_3 = 0$  in equation (15). The values for the rest of the EOS parameters used as input data to represent the aluminum alloys considered in this study, along with the corresponding references, are provided in Table 2. The first order volume correction factor (a) in equation (17) was assumed to be equal to zero.

It should be noted that due to the lack of EOS parameters specific to Al2017-T4 and owing to the metallurgical proximity of these two alloys (see Table 1), the corresponding parameters of this alloy have been substituted using the data available from the literature for Al2024-T3. Also, as will be discussed in the next section, thin honeycomb walls were modeled using shell elements and, thus, specification of EOS parameters for Al5052-H34 (honeycomb core material) was not required.

Table 1 – Composition of Al2017-T4 and Al2024-T3 alloys

Element	Al, %	Cr,%	Cu, %	Fe, %	Mg, %	Mn, %	Si, %	Ti, %	Zn, %	Other, %
Al2017-T4	91.5-95.5	$\leq 0.10$	3.5 - 4.5	$\leq 0.70$	0.40-0.80	0.40-1.00	0.20-0.80	$\leq 0.15$	$\leq 0.25$	$\leq 0.15$
Al2024-T3	90.7-94.7	$\leq 0.10$	3.8 - 4.9	$\leq 0.50$	1.20-1.80	0.30-0.90	$\leq 0.50$	$\leq 0.15$	$\leq 0.25$	$\leq 0.15$

### 2.2.3 Strength model

The Johnson-Cook model (\*MAT\_015/\*MAT\_JOHNSON\_COOK in LS-DYNA [56]) was used to represent the behavior of the Al2017-T4 and Al6061-T6 alloys. This material model is a typical choice for metals subjected to high strains, high strain rates, and high temperatures. The yield (flow) stress of a material in this model is represented as

$$Y = [A + B \cdot \epsilon_p^n] \cdot [1 + C \cdot \ln \dot{\epsilon}_p^*] \cdot [1 - T_H^m] \quad (18)$$

Here

- $\epsilon_p$  is the effective plastic strain;
- $\dot{\epsilon}_p^*$  is the normalized effective plastic strain rate;
- $T_H$  is the homologous temperature ( $T_H = \frac{T - T_{room}}{T_{melt} - T_{room}}$ );

- A is the initial yield strength;
- B is the hardening constant;
- C is the strain rate constant;
- n is the hardening exponent; and
- m is the thermal softening exponent.

In the Johnson-Cook plasticity model, the calculation of plastic strain is based on the von Mises yield surface and the associated flow rule. The expression in the first brackets of the equation (18) gives the yield stress as a function of plastic strain; the second set of brackets represents the effects of strain rate on stress; and the third set of brackets determines thermal softening of a material. It should be noted that as the temperature reaches the melting temperature of the material ( $T_{\text{melt}}$ ), its yield strength drops to zero.

For modeling the high-rate response of the Al2017-T4 sphere, the Johnson-Cook model parameters readily available from the literature for Al2024-T3 [57] were adopted owing to its metallurgical proximity to Al2017-T4. For Al6061-T6, the Johnson-Cook model parameters specific to this alloy were adopted from [58]. The corresponding material properties are provided in Table 2. Materials of projectile and facesheets considered as failed (no tensile stresses allowed), if tensile pressure exceeded a limit of 2000 MPa, which is consistent with the findings reported [59].

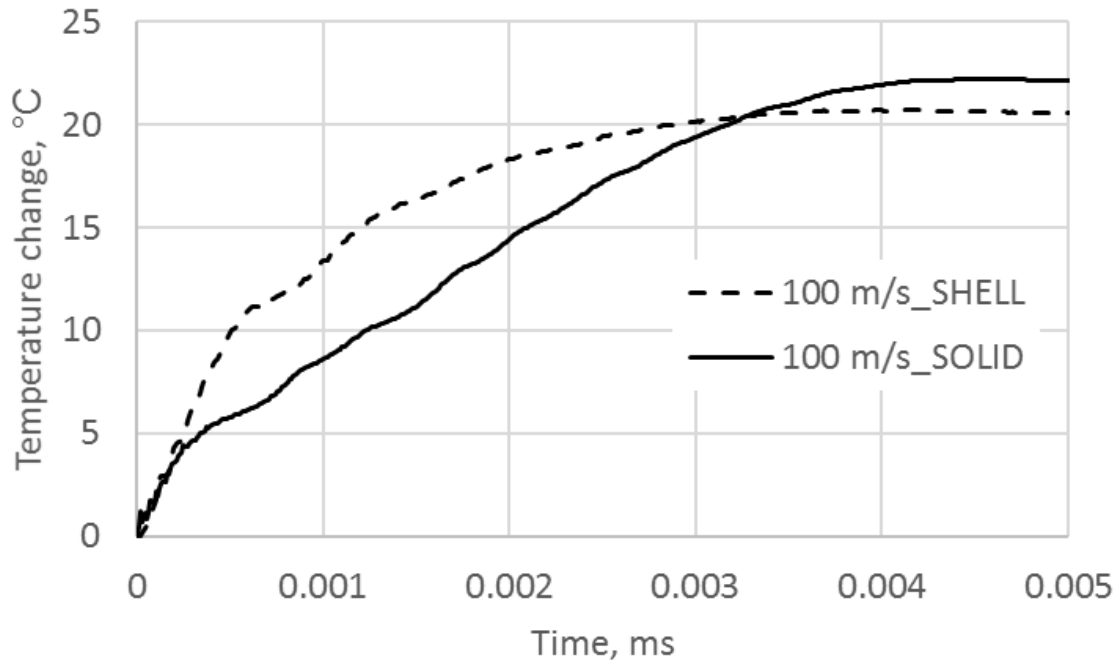
Due to the computational efficiency reasons, meso-scale modeling of honeycomb core was conducted using shell elements. However, using shells, while making the model more robust, places limitations on the capability to account for certain physical phenomena. In particular, local softening of the honeycomb material due to adiabatic temperature increase cannot be computed properly, as calculated plastic work (converts into heat and determines the local temperature change) would not take into account through-the-thickness deformations when shell elements are used. This is illustrated in Figure 12, which presents results of a 1 mm particle impact on a 0.1 mm-thick plate (thickness of the same order as honeycomb wall) modeled with \*MAT\_015 (Johnson-Cook). As can be deduced from the figure, at lower speed (100 m/s) predictions are consistent between the shell and the solid models; however, at higher velocity (1000 m/s), the difference in local

temperature predictions is dramatic. Considering the high-speed nature of the problem, using temperature-dependent material models – such as Johnson-Cook, – with shell elements, could result in over predicting of the flow stress of the material (due to under predicted thermal softening) and, thus, deemed to be impractical. Instead, the material of the core was assumed to be soft enough at yielding to be represented using an elastic-perfectly plastic model (\*MAT\_003/\*MAT\_PLASTIC\_KINEMATIC in LS-DYNA). As will be shown in the following sections, this approach, while being very simplistic, allowed to achieve a good correlation with experimental data. A specific set of material properties used for Al5052-H34 was as follows:  $E = 70.3$  GPa,  $\nu = 0.33$ ,  $\sigma_Y = 193$  MPa,  $E_{tan} = 0.0$  GPa. In addition, a simple effective plastic strain criterion was used to establish a failure limit and remove failed shell elements from the simulation, allowing fragments to penetrate into adjacent cells.

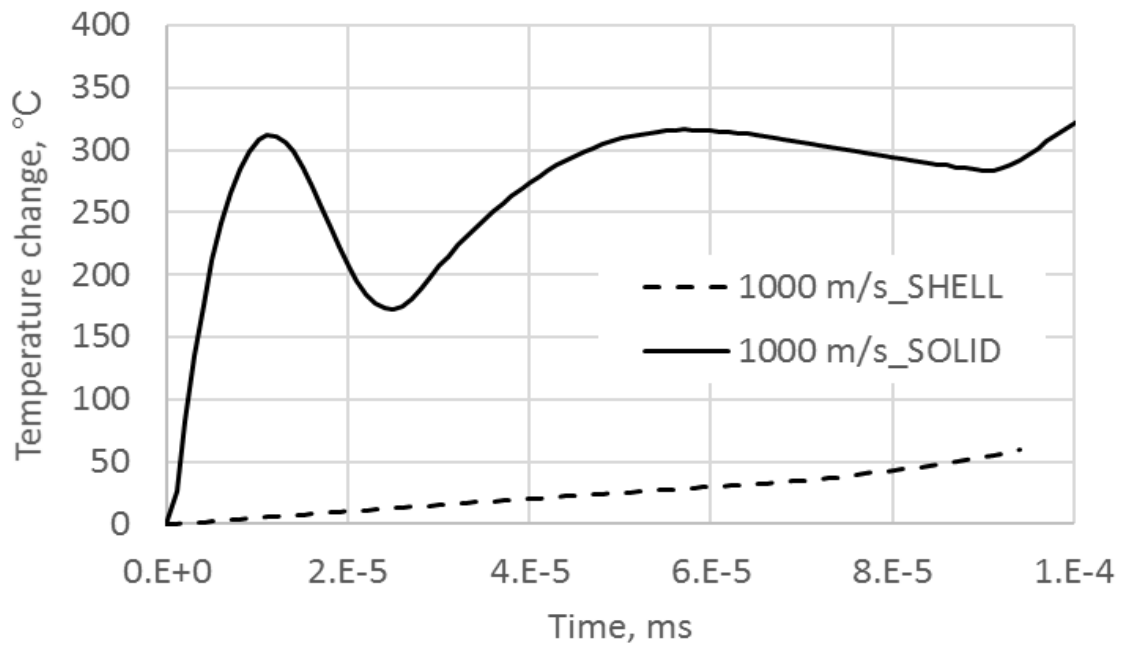
Table 2 – Material model parameters used to represent Al2017-T4 and Al6061-T6 in simulations

Material	Model component	Component name	Material properties					Reference
Al2017-T4	Equation of state	Gruneisen	$\rho$ , kg/m <sup>3</sup>	$C$ , mm/ms	$S_1$	$Y_0$	$a$	[55]
			2780	5328	1.338	2.00	0.0	
	Strength model	Johnson-Cook	$A$ , MPa	$B$ , MPa	$n$	$C$	$m$	[57]
			265	426	0.340	0.0150	1.000	
Al6061-T6	Equation of state	Gruneisen	$\rho$ , kg/m <sup>3</sup>	$C$ , mm/ms	$S_1$	$Y_0$	$a$	[60]
			2703	5240	1.400	1.97	0.0	
	Strength model	Johnson-Cook	$A$ , MPa	$B$ , MPa	$n$	$C$	$m$	[58]
			324	114.0	0.420	0.0020	1.340	





**100 m/s impact**



**1000 m/s impact**

Figure 12 – Temperature rise, as predicted by the Johnson-Cook model in simulations with shell and solid elements at two different impact velocities

### 2.3 Numerical model

The impact conditions considered in this study involved normal angle collisions between a panel and a projectile, which are known to be the most conservative design scenarios for HCSPs due to the so-called *channeling effect of honeycomb core*, when honeycomb cells constrain expansion of the cloud of high-speed projectile fragments, focusing the fragments' impact energy and momentum on a small area on the rear face sheet, as was exemplified in Fig. 4 (b).

The hypervelocity impact simulation model of a honeycomb-core sandwich panel developed by the authors in LS-DYNA simulation software is shown in Figure 13–16. The panel was represented by 1.3 mm-thick facesheets and 50.8 mm-thick core. In-plane size of the modeled piece was 70 mm  $\times$  70 mm. In the impact region, discretization of all parts involved 0.1 mm elements or SPH particles, which is consistent with the findings of the earlier study by Legaud et al. [59]. The particular setup illustrated in Figure 13–16 (with a spherical 2.5 mm projectile) replicates the conditions of the NASA experiment described in Ref. [61] and denoted as HITF 9005, which was used in this study to verify the developed numerical model. A detailed description of the different parts of the model, as well as the methods used to describe those parts, is provided below.

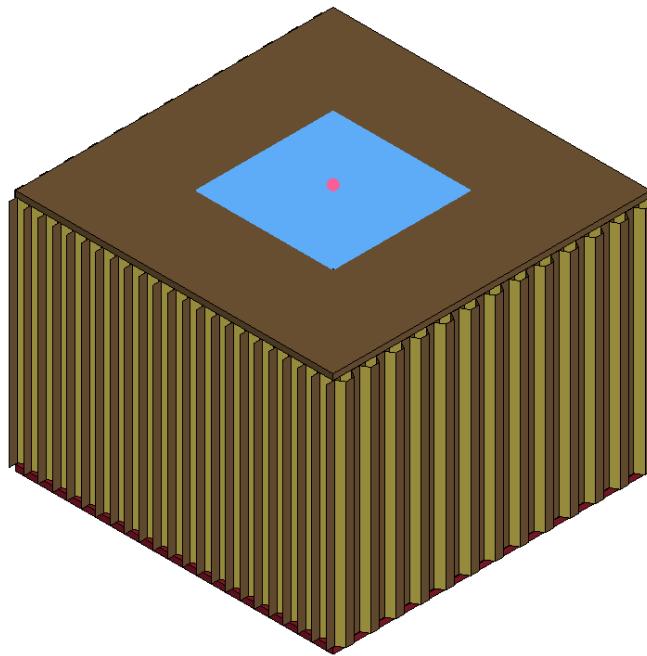


Figure 13 – Isometric view of the developed HVI simulation model

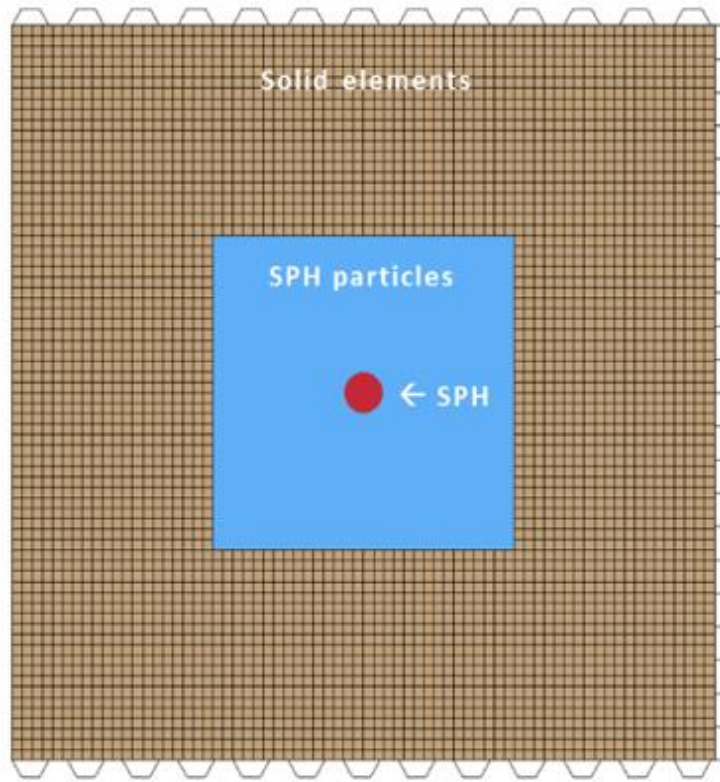


Figure 14 – Top view of the developed simulation model

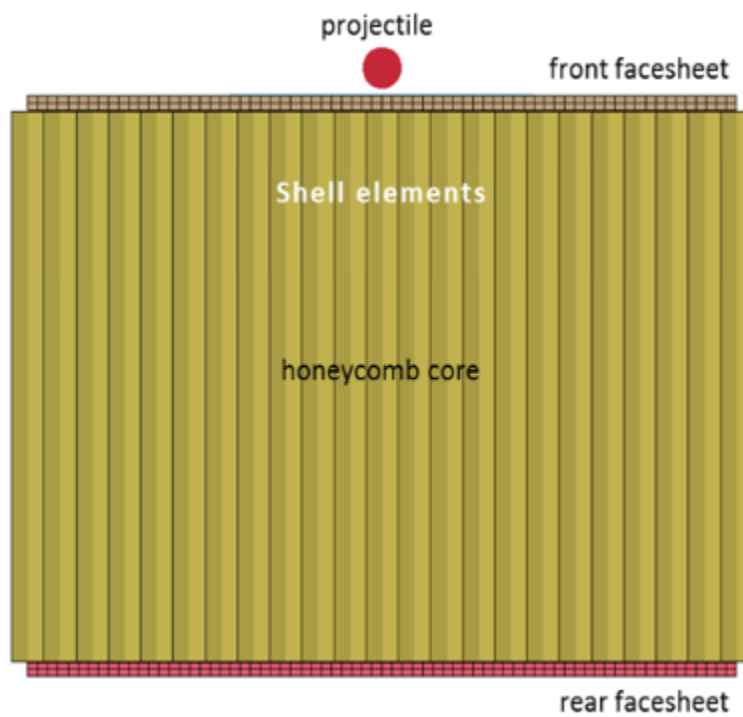


Figure 15 – Front view of the developed simulation model

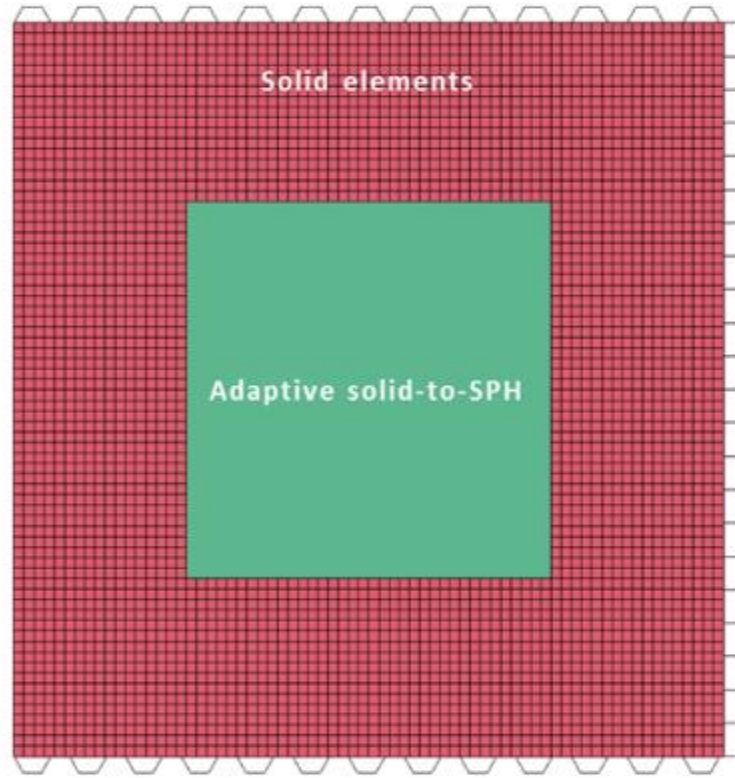


Figure 16 – Rear view of the developed simulation model

*Projectile.* Since a projectile, as a result of hypervelocity collision with a sandwich panel, was expected to experience a complete disintegration, fragmentation, and be subjected to extremely high deformations, a meshless method – smoothed particles hydrodynamics (SPH) – was employed to represent this part of the simulation model. Projectiles of different geometries have been modeled in this study, however, a common particle size of 0.1 mm has been used for the discretization of all considered projectile types. An Eulerian SPH formulation # 0 [62], which was found in [59] to provide the highest accuracy in HVI simulations, was used in all cases throughout this study. It was used with the quadratic spline kernel function, designed to relieve the compressive instability of SPH in HVI problems.

*Front facesheet.* The front facesheet representation employed both finite elements and SPH particles, as shown in Figure 15. In particular,  $30 \times 30$  mm central region, where large deformations can be caused by the projectile impact, have been fine-discretized using 0.1 mm SPH particles (13 particles through the thickness), while the rest of the front

facesheet has been discretized using  $1.0 \times 1.0 \times 0.65$  mm solid elements (2 elements through-the-thickness of the facesheet). This roughly meshed region around the SPH part was used to prevent the reflection of stress waves from the boundaries of the SPH region. Interaction of the two parts – solid and SPH – has been modeled through the \*CONTACT\_AUTOMATIC\_NODES\_TO\_SURFACE algorithm in LS-DYNA [62]. With this contact algorithm, every “slave” node is checked for penetration through the “master” surface, as illustrated in Figure 17. The contact search algorithm employed by automatic contacts in LS-DYNA makes them well-suited to handling disjoint meshes and particles, which can be important in problems involving large deformations. Interaction between the front wall and the projectile SPH particles was implemented through the standard SPH interpolation.

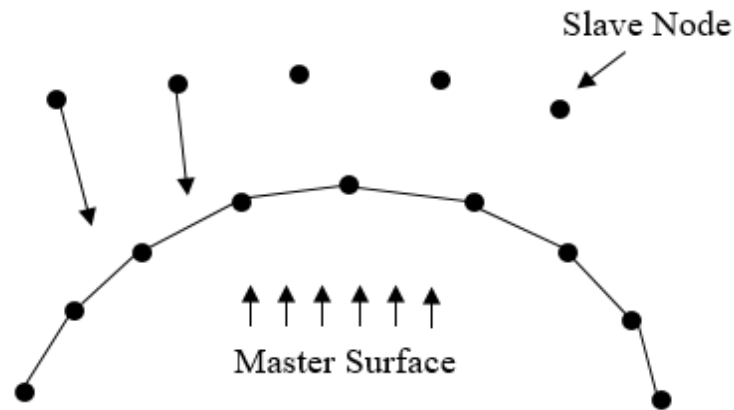


Figure 17 – Schematic picture of NODES\_TO\_SURFACE contact

*Honeycomb core.* The honeycomb cores of the sandwich panels were represented in the simulations explicitly, using fully integrated shell elements (formulation #16 in LS-DYNA with Reissner-Mindlin kinematics, implying that cross-sections remain straight and unstretched, and shear deformations are possible), as exemplified in Figure 18. The explicit representation was employed in order to facilitate modeling of the channeling effect of the honeycomb core on the cloud of hypervelocity fragments.

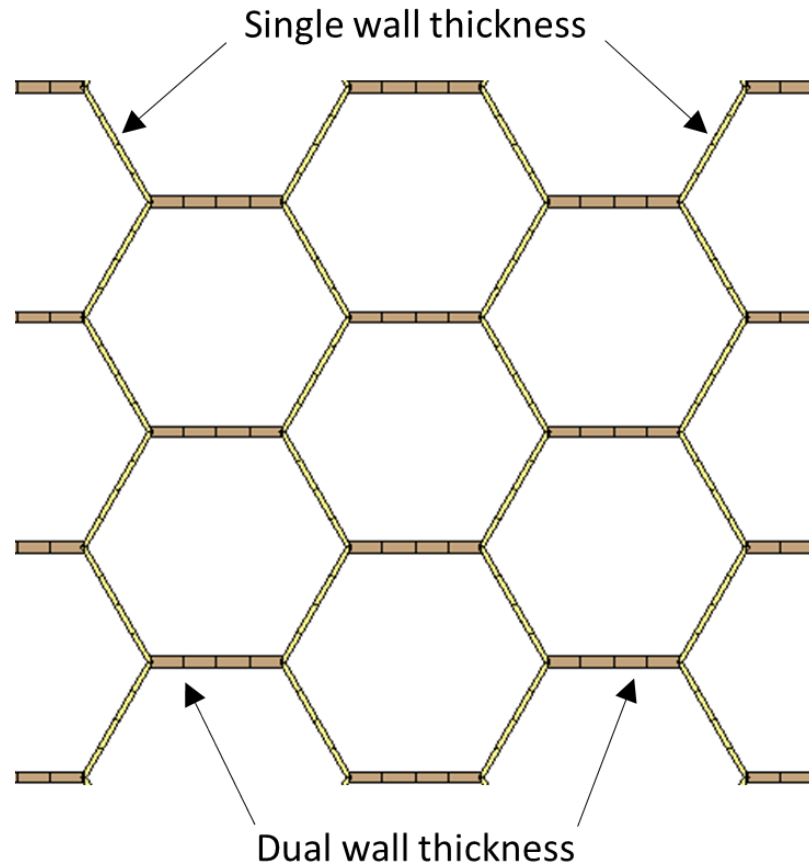


Figure 18 – An explicit representation of a honeycomb core using shell elements  
(visualization shows the “assigned” thickness of the shell elements)

Dimensions of the honeycomb cells corresponded to the HexWeb CR III honeycomb grade by Hexcel [63] with the nominal foil thickness of 0.0762 mm (“single wall” in Figure 18). A foil thickness was assigned to the honeycomb parts (single- and dual-wall) as an attribute of the corresponding shell element section. While the original model replicating the conditions of the NASA HITF 9005 experiment involved a honeycomb with 1/8 inch cells, other cell dimensions were used in subsequent simulations as well, and are represented in Figure 19. Contact between SPH particles and the shell element-modeled honeycomb core was implemented using the \*CONTACT\_AUTOMATIC\_NODES\_TO\_SURFACE algorithm in LS-DYNA.

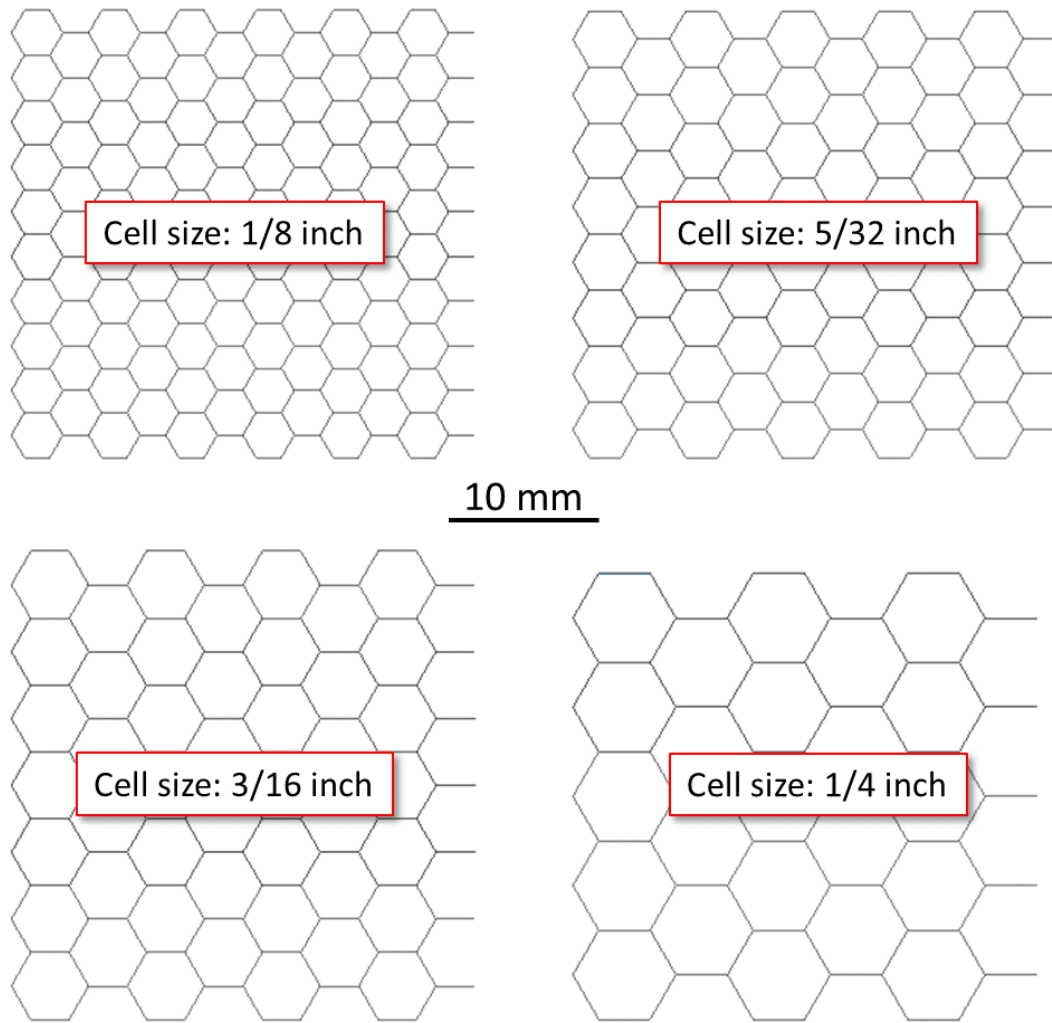


Figure 19 – Comparison of different honeycomb cell sizes used in this study

*Rear facesheet.* It is well known that while the SPH technique is often advantageous in modeling scenarios involving extreme deformations and fragmentation, the finite element method (FEM) in its Lagrangian implementation is well-suited for tracking the materials' interfaces. To use the advantages of both techniques simultaneously, a hybrid FEM/SPH approach was implemented for the facesheets using the LS-DYNA's \*DEFINE\_ADAPTIVE\_SOLID\_TO\_SPH keyword, which allowed local and adaptive transformation of Lagrangian solid elements (formulation #1) to SPH particles when the solid elements became highly distorted and inefficient. Such conversion was triggered by the erosion of solid elements which happened when the effective plastic strain in the element reached the level of 30%. The SPH particles replacing the eroded solid elements

inherited all the nodal and integration point quantities of the original solids and initiated being attached to the neighboring solid elements. This approach makes it possible to accurately capture different levels of rear wall damage: from small deformations (using solid elements) to very large deformations, converting, if needed, distorted solid elements to SPH particles. The interaction between SPH-modeled projectile and front facesheet fragments and the solid elements of the rear facesheet was simulated using an eroding nodes-to-surface contact – the \*CONTACT\_ERODING\_NODES\_TO\_SURFACE\_MPP algorithm in LS-DYNA. Logic of this contact algorithm allows the contact surface to be updated as exterior elements are deleted.

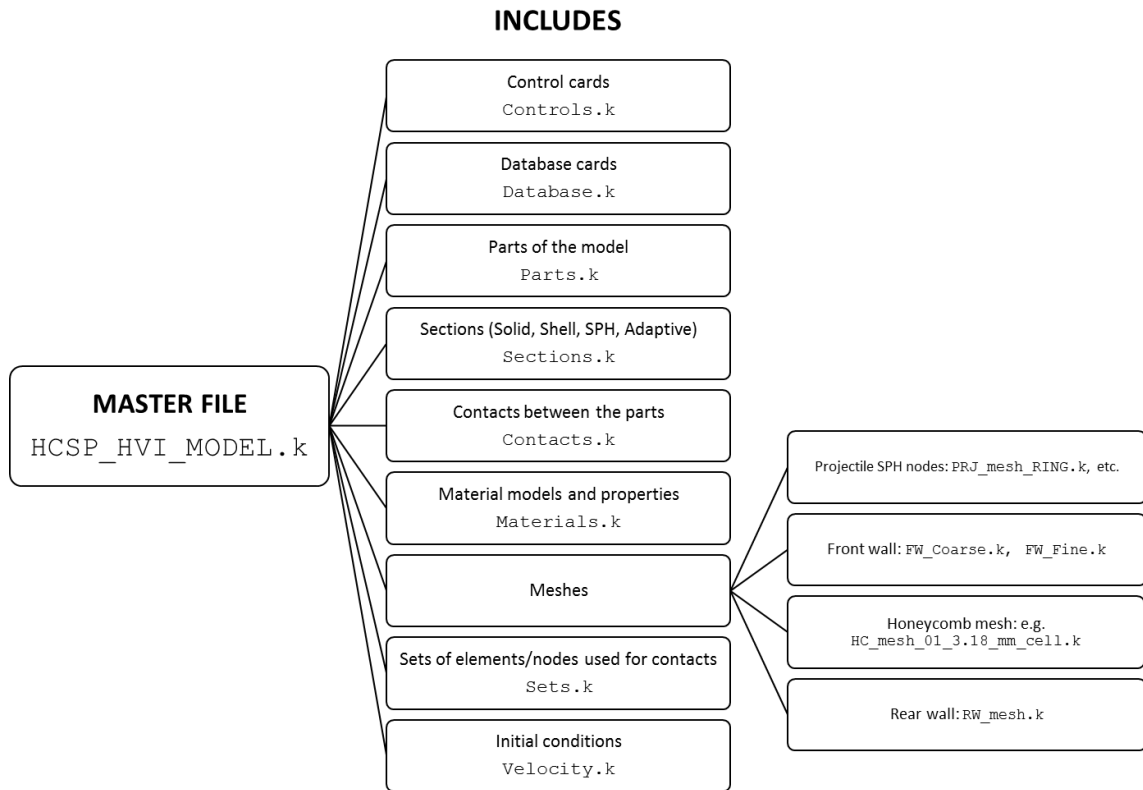


Figure 20 – Structure of the developed simulation model for HVI on HCSP

For different functions, LS-DYNA utilizes “keywords” with pre-defined arguments organized into “cards”. For example, a keyword \*NODE would create a node with coordinates defined by the arguments of the keyword listed within its card. LS-DYNA input file (“the model”) lists all keywords and cards used to create the model, saved as a “keyword file” that has an extension .k. To make the input file easy to maintain, the model



developed in this study was split into subfiles (“includes”), each containing keywords with a common function. For example, include `Materials.k` contains keywords, cards, and parameters of all materials used in the model. Finally, the “master file” lists and references all includes containing model data. The corresponding structure of the developed simulation model is shown in Figure 20. The content of the master and all include files is provided in the Appendix. It should be noted that separate includes were developed for different honeycomb grades (see Figure 19) and projectile topologies (sphere, disk, ring) and dimensions. This allowed to change projectile and honeycomb core in the model by simply changing the name of the corresponding include file in the master file.

All hypervelocity impact simulations were conducted using a massively parallel processing (MPP) solver of LS-DYNA on a computer with twelve Intel Core i7-8700 CPUs and 32 GB of RAM. With these computational resources and for simulations involving 40  $\mu$ s after impact initiation, an average simulation runtime was around 40 hours. Overall, it took around 600 hours of machine time to conduct all simulations reported in this study.

## 2.4 Summary of Chapter 2

A numerical model was developed for simulating hypervelocity impacts of orbital debris on a honeycomb-core sandwich panel with aluminum core and facesheets.

In the model, behavior of aluminum alloys (except Al5052, the material of the honeycomb core) was represented using a combination of the Gruneisen equation of state and the Johnson-Cook strength model. For the honeycomb core, a simple elasto-perfectly plastic model and no EOS were utilized due to the limitations imposed by shell elements used to discretize the core.

The following techniques were employed to represent the parts of the model:

- Smoothed particles hydrodynamics (SPH) – for modeling of the projectile and the central part of the front facesheet;
- Finite element method (FEM), solid elements – for representing the front and the rear facesheets in the regions away from the impact location;

- Finite element method (FEM), shell elements – for the computationally efficient representation of the honeycomb core;
- Adaptive FEM-to-SPH method – for modeling of the rear facesheet in the area where impact damage was expected.

The simulation model was implemented as a master file referencing multiple include files, each containing keywords and cards with a common logical function. The model was developed for the MPP version of LS-DYNA.

### 3: RESULTS AND DISCUSSION

#### 3.1 Validation of the simulation model

Validation of the developed simulation model was achieved by comparison of its predictions with

- a) the results of the physical experiment (HITF 9005) conducted by NASA and reported in Ref. [61]; and
- b) predictions of a ballistic limit equation (BLE) – an empirical predictive model developed by Schaefer Ryan and Lambert and adjusted using approximately 200 impact tests, including multiple HVI experiments with aluminum honeycomb-core sandwich panels (spherical projectiles only) [16].

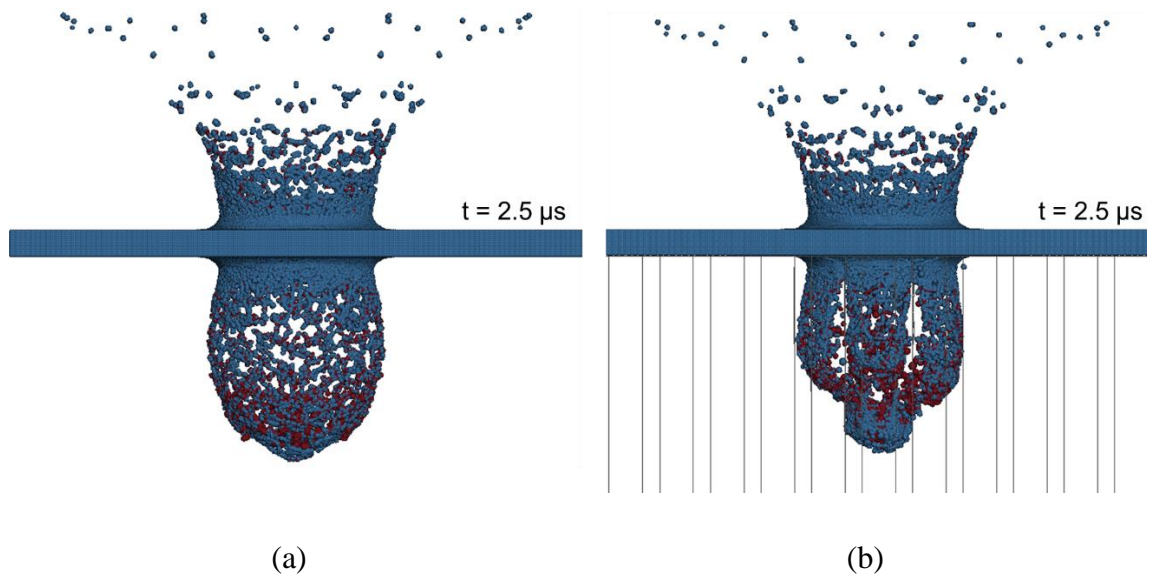


Figure 21 – Predicted shape of the fragment cloud in case of 6.91 km/s collision of a 2.5 mm Al2017-T4 projectile with 1.3 mm-thick Al6061-T6 plate: (a) honeycomb is lacking; and (b) honeycomb is present

Prior to quantitative validation, the model was evaluated – qualitatively – for its ability to represent channeling of the fragment cloud by the honeycomb core. As described in the previous section, channeling represents a phenomenon in which honeycomb cells constrain the expansion of the cloud of high-speed projectile fragments, focusing the impact energy and momentum of the fragments onto a small area of the rear face sheet.

This effect is illustrated in Figure 21, where the results of two simulations – with and without the honeycomb and equivalent in all other aspects – are compared. As can be deduced from the figure, the shape of the fragment cloud in the second case (Fig. 21(b)) clearly demonstrates the presence of fragments confined within the honeycomb cells and is significantly different from the case when the expansion is not impeded by the core (Fig. 21(a)). In addition, Figure 22 demonstrates the evolution of the channeled fragment cloud, depicting its shape at two different moments of time.

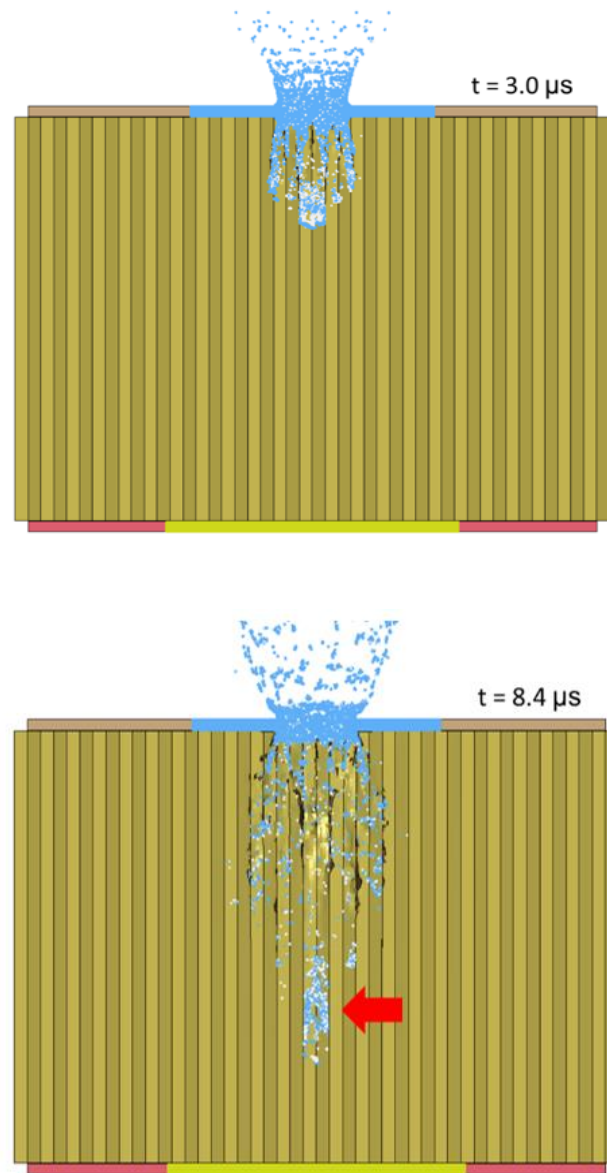


Figure 22 – Channeling of hypervelocity fragments by honeycomb cells (sectioned view)

The physical experiment used for validation of the simulation model was conducted by NASA and reported in Ref. [61]. In this test, a 6.91 km/s 2.5 mm Al2017-T4 spherical projectile hit a honeycomb panel with 1.3 mm-thick Al6061-T6 facesheets separated by a 50.8 mm-thick 1/8-5052-0.003 honeycomb core. Comparison of the simulation results with the physical HVI experiment conducted by NASA is represented in Figure 23 – 25 for the front facesheet, core, and rear facesheet damage, respectively. It can be seen that the 6.91 km/s sphere of the above-critical diameter induced full perforation of the sandwich panel, creating a near-circular entrance hole in the front facesheet and an irregular-shaped exit hole in the rear facesheet. The specific validation metrics included the following parameters: a) size (diameter) of the hole in the front facesheet; and b) size (effective diameter) of the hole in the rear facesheet. Comparison of the numerical values for the validation metrics is provided in Table 3. In addition, Table 3 includes an estimate of the entrance hole diameter obtained for the same impact conditions using an analytical model by Jolly and Schonberg [64]. As can be deduced from the table, predictions of the developed simulation model agree very well with the experimental and analytical results.

Table 3 – Predictions of the developed simulation model, compared with the available experimental and analytical data

<b>Part</b>	<b>#</b>	<b>Data source</b>	<b>Hole diameter, mm</b>	<b>Error, %</b>	<b>Reference</b>
Front facesheet	1	NASA Experiment HITF 9005	6.9 (7.0 x 6.8)	--	[61]
	2	Analytical model by Jolly & Schonberg	6.8	-1.5	[64]
	3	UWindsor simulation	7.1	+2.9	UWindsor data
Rear facesheet	1	NASA Experiment HITF 9005	4.4* (4.7 x 4.2)	--	[61]
	2	UWindsor simulation	4.1* (4.0 x 4.2)	-6.8	UWindsor data

\* Effective hole diameter calculated as  $D_{\text{hole}} = 2\sqrt{A_{\text{hole}}/\pi}$ , where  $A_{\text{hole}}$  is the exit hole area

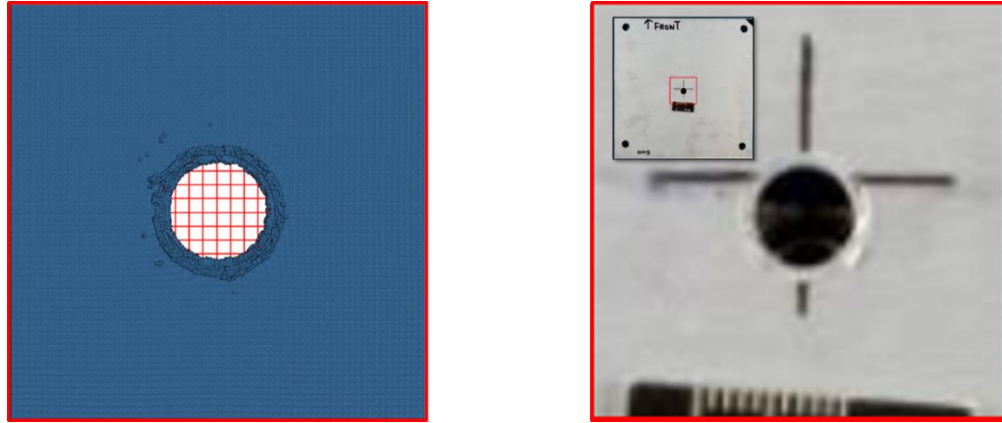


Figure 23 – Front wall damage: simulation (red grid cell is  $1 \times 1$  mm) vs. NASA experiment (HITF 9005, [61])

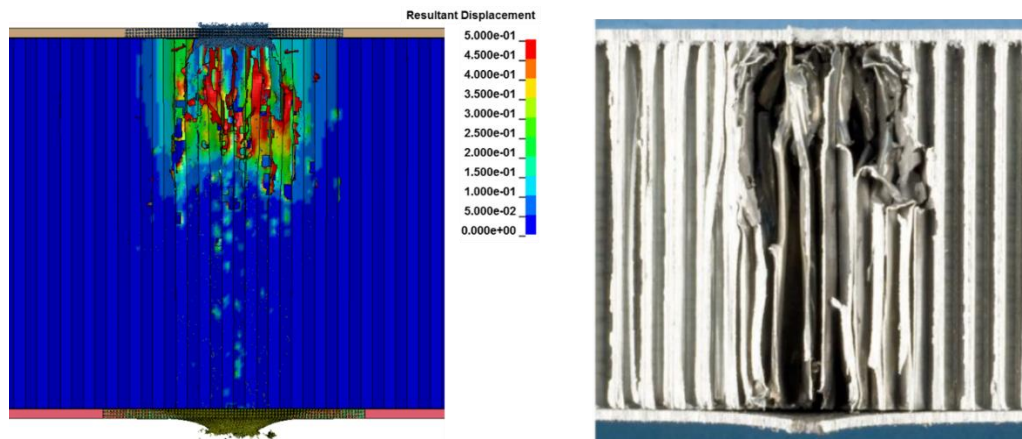


Figure 24 – Honeycomb damage: simulation vs. NASA experiment (HITF 9005, [61])

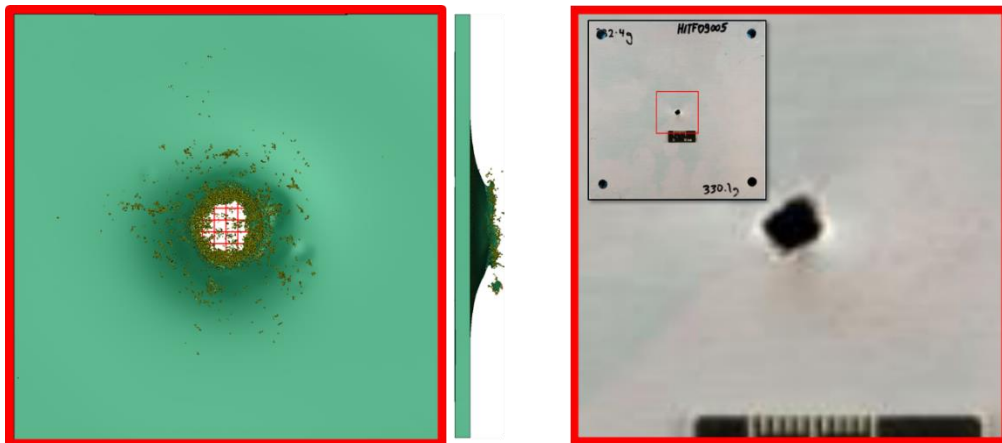


Figure 25 – Rear wall damage: simulation (red grid cell is  $1 \times 1$  mm) vs. NASA experiment (HITF 9005, [61])

Capabilities of the developed simulation model to predict ballistic limits of the honeycomb-core sandwich panels was evaluated by comparison of its predictions with those of the well-verified ballistic limit equation proposed by Schaefer Ryan and Lambert, which was adjusted by its authors using approximately 200 spherical projectile HVI tests, including multiple experiments with aluminum HCSPs [16]. In case of normal impact of an aluminum projectile with the speed equal to or exceeding 7 km/s on all-aluminum HCSP, the SRL BLE can be represented by the equation (19):

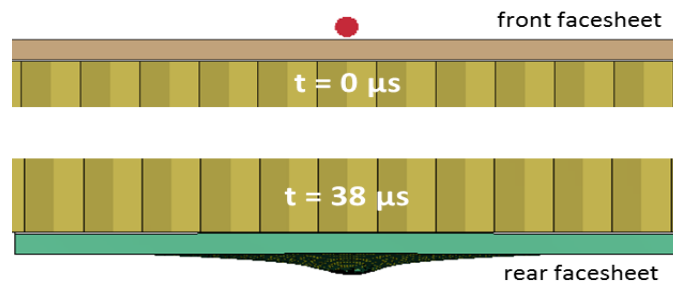
$$D_{cr} = 1.155 \cdot \sqrt[3]{\frac{t_{HC} \cdot t_{RW}^2}{K_{3D}^2 \cdot \rho_p \cdot \rho_{FW}^{1/3} \cdot v_p^2}} \cdot \left(\frac{\sigma_{Y,FW}}{70}\right) \quad (19)$$

In this expression:

- $t_{HC}$  and  $t_{RW}$  are the honeycomb core and the rear facesheet (“rear wall”) thicknesses, respectively [cm];
- $\rho_p$  and  $\rho_{FW}$  are the projectile and the front facesheet (“front wall”) densities, respectively [g/cm<sup>3</sup>];
- $v_p$  is the projectile speed [km/s];
- $\sigma_{Y,FW}$  is the yield stress of the front facesheet material [ksi]; and
- $K_{3D}$  is the BLE fit factor, which is equal to 0.4 in the case of aluminum-on-aluminum impacts.

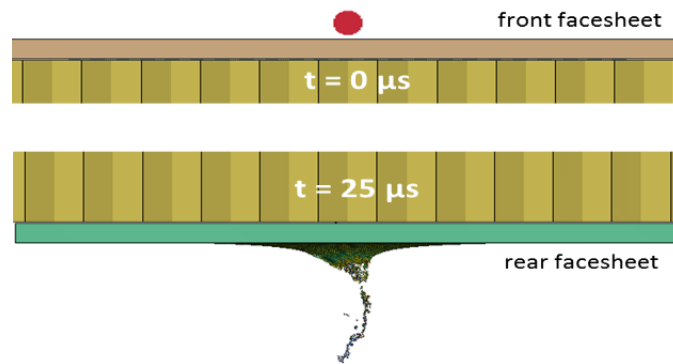
Substituting the parameters of the panel ( $\rho_{FW} = 2.70$  g/cm<sup>3</sup>,  $t_{HC} = 5.08$  cm,  $t_{RW} = 0.13$  cm,  $\sigma_{Y,FW} = 40$  ksi) and the projectile ( $\rho_p = 2.78$  g/cm<sup>3</sup>,  $v_p = 7.0$  km/s) in (9), the critical projectile diameter was estimated as  $D_{cr} = 0.136$  cm = 1.36 mm.

$$D_p = 1.2 \text{ mm } (D_p < D_{cr, BLE})$$



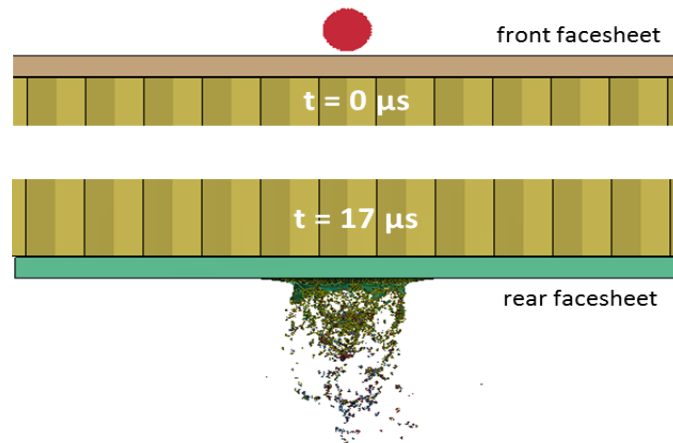
(a)

$$D_p = 1.5 \text{ mm } (D_p > D_{cr, BLE})$$



(b)

$$D_p = 2.5 \text{ mm } (D_p \gg D_{cr, BLE})$$



(c)

Figure 26 – Predicted rear facesheet damage as a function of projectile diameter



In order to validate the simulation model against the prediction of the BLE, two simulations were run: one with slightly (approx. 10%) smaller projectile diameter than the BLE-predicted  $D_{cr}$ , and another – with slightly (approx. 10%) larger projectile diameter than the BLE-predicted  $D_{cr}$ . The validation metrics in this case was the capability of the model to detect no-perforation of the rear facesheet in the former case ( $D_p < D_{cr}$ ), and to show the clear perforation in the latter case ( $D_p > D_{cr}$ ). Results of these simulations are shown in Figure 26, which, for comparison, also illustrates the case of  $\sim 2 \times D_{cr}$  (2.5 mm) projectile impact.

As can be deduced from Fig. 26 (a) and (b), the predictions of the numerical model are consistent with the SRL BLE calculations: the sub-critical projectile does not perforate the rear facesheet even long after the impact (analysis progressed up to 38  $\mu s$ ), while with the slightly above-critical projectile diameter, the perforation is noticeable after about 25  $\mu s$ . For comparison (Fig. 26 (c)), in case of  $D_p \gg D_{cr}$ , the full perforation of the front facesheet happens as early as at 15-17  $\mu s$  after impact initiation.

### 3.2 Projectile shape effects

As discussed in the introduction section, disk-like penetrators with high pitch have been found to be among the most dangerous projectile shapes for the single-purpose dual-wall (Whipple) shields. In this study, the verified HVI simulation model was used to extend this analysis for the case of high-pitch disk-like projectile impacts on the multi-purpose shields – the honeycomb-core sandwich panels (analyses employed the panel with ballistic limit established in Section 3.1). In addition to the computations with spherical projectiles, used as a reference, simulations were conducted with such shapes as simple disk-like impactors and projectiles with the shape represented by a disk with the central hole. The latter will be referred to as “ring-shaped” impactors. The three projectile shapes considered in this study, along with their characteristic parameters, are illustrated in Figure 27.

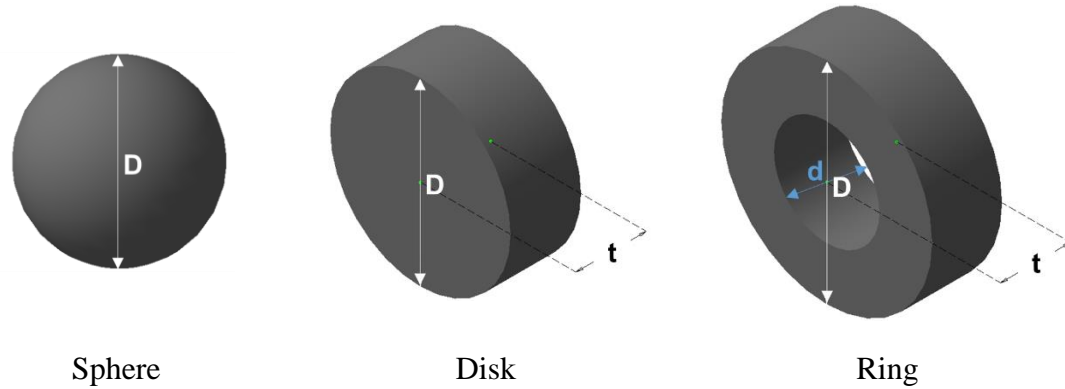


Figure 27 – Equal-volume sphere, disk and ring projectiles

Spherical projectiles were characterized by diameter ( $D$ ), disk projectiles – by diameter ( $D$ ) and thickness ( $t$ ), and ring projectiles – by thickness ( $t$ ), outer diameter ( $D$ ), and the ratio of the inner and the outer diameters ( $K$ ). The latter was kept constant and equal to 0.5 for all ring projectile shapes used. The investigation considered disk and ring impactors with different aspect ratios, defined as a ratio of the outer diameter to the thickness of a projectile  $AR = D/t$ . Dimensions of all projectiles are listed in Table 4.

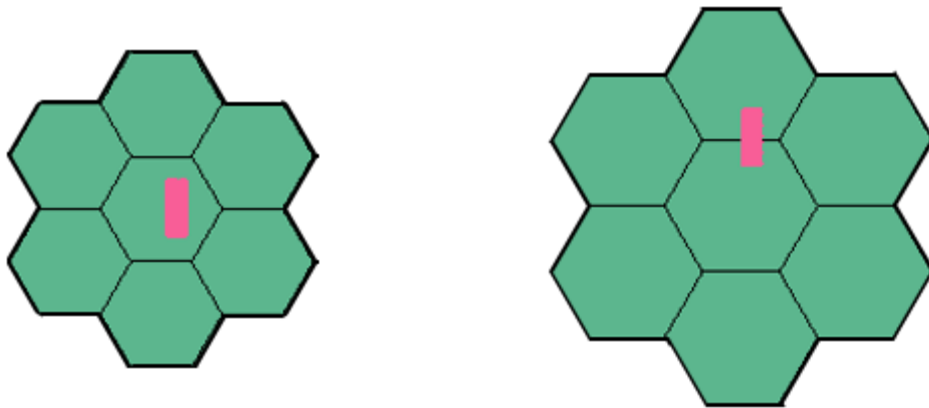
Table 4 – Parameters of the projectiles used in this study

Type	Aspect ratio	$D$ , mm	$K = d/D$	$t$ , mm	$V$ , mm <sup>3</sup>
Sphere	—	1.50	—	—	1.77
Sphere	—	1.20	—	—	0.90
Disk	1.50	1.20	—	0.80	0.90
Disk	3.00	1.51	—	0.50	0.90
Disk	4.50	1.73	—	0.38	0.90
Ring	1.50	1.32	0.5	0.88	0.90
Ring	3.00	1.66	0.5	0.55	0.90
Ring	4.50	1.90	0.5	0.42	0.90
Ring	3.00	1.53	0.5	0.51	0.70

The test matrix contained 12 numerical experiments, including the two simulations with the sub-critical (1.2 mm) and above-critical (1.5 mm) spherical projectiles that were described in the previous section and were used to verify the model and establish ballistic

limit of the sandwich panel. Specific objectives of the calculations included the following three goals:

1. Understand the perforating ability of disk and ring-shaped projectiles as compared to spherical impactors of the same mass;
2. Evaluate the effect of aspect ratio on the perforating ability of disk and ring shapes;
3. Investigate the effects of projectile-honeycomb cell alignment and honeycomb cell size on ballistic performance of honeycomb core sandwich panels, when hit with non-spherical projectiles.



Projectile aligned with the cell center

Projectile aligned with the cell wall

Figure 28 – Projectile-honeycomb cell alignment

To achieve the first and the second goal, simulations were conducted with disk and ring projectiles of different aspect ratios, varying from 1.5 to 4.5. These projectiles had the same volume (and mass) as the sub-critical spherical projectile with  $D = 1.2$  mm that could not perforate the HCSP with the 1/8 inch-cell honeycomb core (see Section 3.1). For the third goal, HVI simulations were conducted for panels with different honeycomb cores (see Figure 19) and different alignments between the projectiles and the honeycomb cells. This included projectiles roughly centered at the cell center and those aligned with a wall of the honeycomb before impact, as illustrated in Figure 28. The corresponding virtual test matrix is provided in Table 5 and, in addition to the projectile and honeycomb parameters, includes the information about the projectile-honeycomb cell alignment, and the outcome of each test. The latter is defined via a binary pass/fail output, where “fail” corresponds to

full perforation of the panel's rear facesheet. Termination time for all simulations was set to 40  $\mu$ s.

Table 5 – Test matrix and outcomes of the numerical experiments

Simulation #	Projectile	Volume, mm <sup>3</sup>	Aspect ratio	HC cell size, inch	Projectile-cell alignment	Outcome
1	Sphere	1.77	—	1/8	center	Fail
2	Sphere	0.90	—	1/8	center	Pass
3	Disk	0.90	1.50	1/8	center	Pass
4	Disk	0.90	3.00	1/8	center	Pass
5	Disk	0.90	4.50	1/8	center	Pass
6	Ring	0.90	1.50	1/8	center	Fail
7	Ring	0.90	3.00	1/8	center	Fail
8	Ring	0.90	4.50	1/8	center	Fail
9	Ring	0.90	3.00	5/32	wall	Pass
10	Ring	0.90	3.00	3/16	center	Pass
11	Ring	0.90	3.00	1/4	wall	Pass
12	Ring	0.70	3.00	1/8	center	Pass
13	Ring	0.90	3.00	1/8 (thinner foil)	center	Pass

Figure 29 shows the setup and the results of simulations 3 – 8 (as denoted in Table 5). As can be deduced from the figure, all simulations with disk impactors resulted in the same outcome as the simulation conducted with the equal-volume (and mass) 1.2 mm spherical projectile: no perforation of the rear facesheet was detected. Changing the aspect ratio of the disk projectiles in the range of 1.5 – 4.5 did not have any noticeable effect on their penetrating ability. The opposite is true for the ring-shaped impactors. All three HVI simulations conducted with the ring projectiles under identical impact conditions resulted in the perforation of the honeycomb-core panel, as depicted in Figure 29. This, for the first time, reveals that ring-shaped impactors may be of higher concern than the simple disk projectiles. This may be a consequence of higher elongation of ring projectiles (for the same volume,  $D_{\text{ring}} > D_{\text{disk}}$ ), as well as a complex interaction of the shock waves with the

internal free boundaries of the ring – altogether leading to lower degree of fragmentation of a ring impactor upon collision with the front facesheet, as compared to the disk-shaped counterpart. The effect of aspect ratio – varied from 1.5 to 4.5 in this study – was moderate. Size of the exit hole in the rear facesheet (the effective hole diameter of an irregular-shaped hole, measured on a 0.1 mm × 0.1 mm grid) was:

- 0.7 mm in case of the projectile with AR = 1.5;
- 0.4 mm for the projectile with AR = 3.0; and
- 0.7 mm, when the projectile with AR = 4.5 was used.

Such nonlinear variation of the hole size may suggest the presence of several competitive mechanisms, which affect penetrating ability of ring projectiles when their aspect ratio is changed.

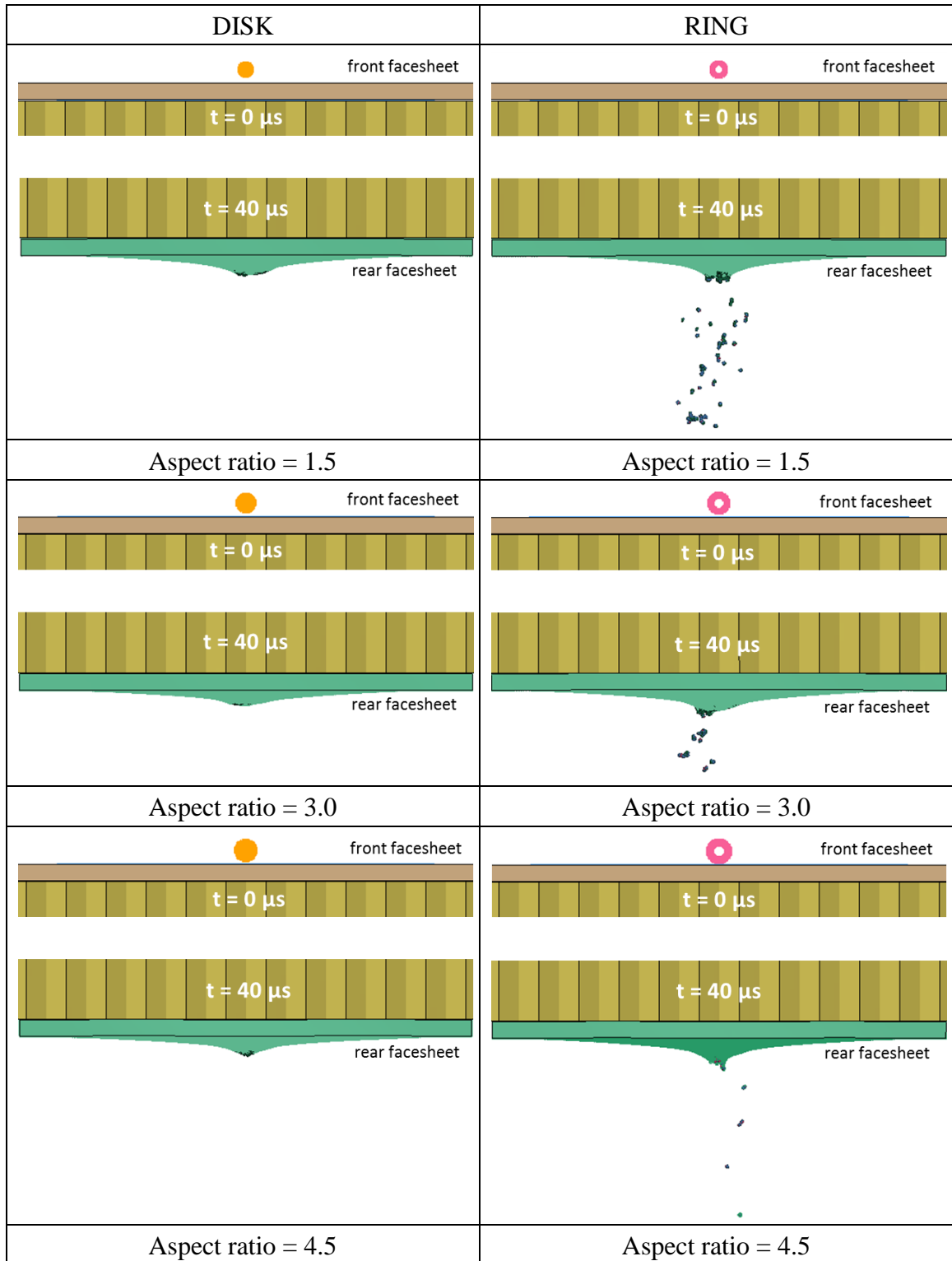


Figure 29 – Effects of projectile shape and aspect ratio on damage to the rear facesheet  
(all projectiles have the same volume of  $0.9 \text{ mm}^3$ )

In order to evaluate the ballistic limit of the reference honeycomb-core sandwich panel (1/8-5052-0.03 50.8 mm-thick honeycomb bonded to 1.3 mm-thick Al6061-T6 facesheets), additional simulation (denoted as simulation # 12 in Table 5) was conducted. In this case, a ring projectile with a reduced volume ( $0.7 \text{ mm}^3$ ) was used. Its outcome – in comparison with a simulation that involved a  $0.9 \text{ mm}^3$  projectile – is shown in Figure 30. As can be deduced from the figure, the former simulation predicted no perforation of the rear facesheet. This allowed to bound the ballistic limit of the honeycomb-core sandwich panel, such that a “critical volume” of a ring projectile must be between  $0.7 \text{ mm}^3$  and  $0.9 \text{ mm}^3$ , i.e. around  $0.8 \text{ mm}^3$ . At the same time, the critical spherical projectile diameter calculated in Section 3.1 was 1.36 mm, which corresponds to a sphere with a volume of  $1.32 \text{ mm}^3$ . In other words, the maximum volume of a ring projectile that can be tolerated by the reference honeycomb-core sandwich panel without failure in case of 7 km/s impact is 1.65 times smaller ( $0.8 \text{ mm}^3$ ) than that of a spherical projectile ( $1.32 \text{ mm}^3$ ).

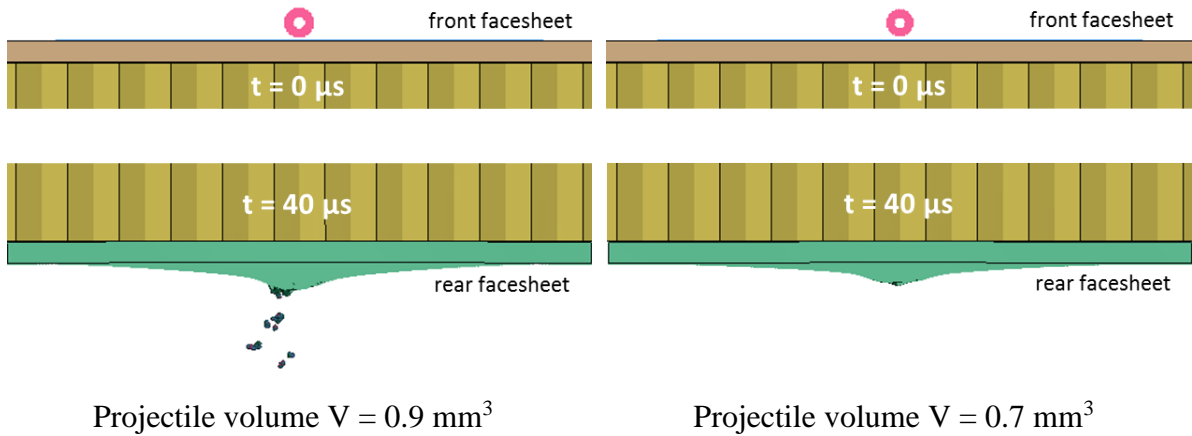


Figure 30 – Ballistic limit of the HCSP in case of the ring projectile impact ( $AR = 3.0$ )

### 3.3 Honeycomb core effects

The effect of honeycomb cell size and projectile/cell alignment on ballistic limit of HCSP was evaluated using a series of simulations with ring projectiles ( $AR = 3.0$ ) that involved, in addition to 1/8 inch cells, honeycomb cores with other cell dimensions, namely 5/32, 3/16 and 1/4 inch (simulations # 7, 9 - 11 in Table 5). The results of these analyses are shown in Figure 31. As can be deduced from this figure, both the cell size and the alignment can influence an outcome of analysis. Cell size effect can be seen through the

comparison of simulations that involved 1/8 and 3/16 honeycomb cores, all other conditions being equal. As a result of 7 km/s impact, the panel with 1/8 inch cells was perforated, while the panel with 3/16 inch cells did not exhibit perforation of the rear facesheet, being able to contain all fragments of the projectile and the front facesheet.

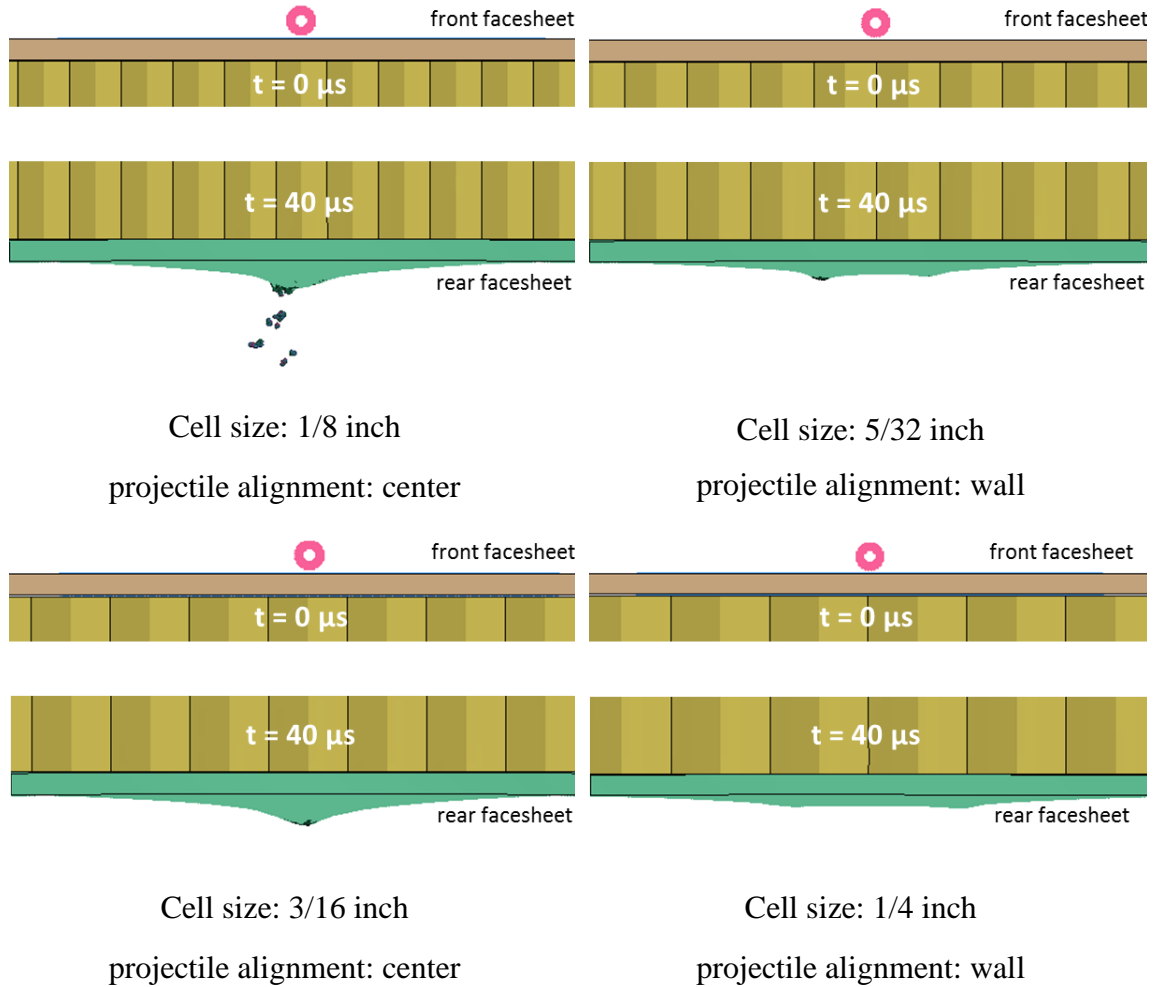


Figure 31 – Effect of honeycomb cell size on rear facesheet damage (all projectiles have the same aspect ratio of 3.0 and volume of  $0.9 \text{ mm}^3$ )

This effect can be simply explained by the additional space provided by larger honeycomb cells for expansion of the cloud of fragments, enhancing distribution of their momentum over a larger area on the rear facesheet (less channeling), thus reducing damage to it. Similar reasoning applies to explain the influence of projectile and honeycomb alignment (“cell center” vs. “wall”) on the rear facesheet damage that is seen in Figure 31. In case of wall-centered impact, projectile fragments are channeled through two



honeycomb cells instead of just one in the case of cell centering. Notably, alignment with the wall not only reduces the severity of damage, but changes its mode as well (two spaced small bulges on the rear facesheet instead of one tall bulge). Apparently, design calculations should consider alignment of a projectile with cell center as a more conservative scenario.

To further illustrate these effects, Figure 32 depicts two extremes in terms of cloud expansion – fragment cloud formed as a result of impact of a cell-centered ring projectile on a 1/8-inch honeycomb core panel (simulation # 7) and the cloud resulting from HVI on HCSP with 1/4 inch cells of the same ring projectile, but aligned with the wall of the honeycomb (simulation # 11). As can be deduced from the figure, the difference in radial expansion of the clouds of fragments varies dramatically between these two cases.

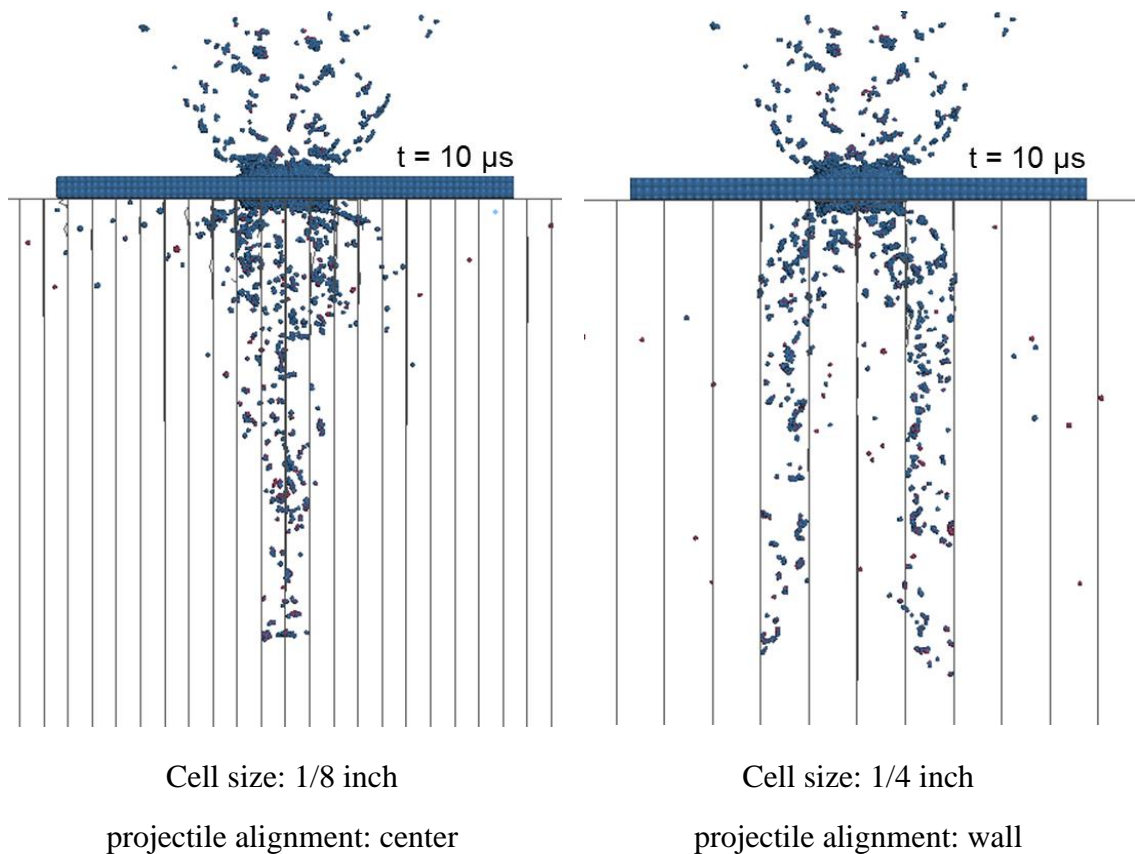


Figure 32 – Cell size and projectile/honeycomb alignment effect on fragment cloud expansion

The effect of honeycomb foil thickness can be seen comparing simulations conducted with 1/8-inch honeycomb cores that had 0.076 mm and 0.025 mm thickness, all other sandwich panel parameters and impact conditions the same (7 km/s “ring” projectile with  $AR = 3.0$ ). The results of these simulations are shown in Figure 33. Using a honeycomb with thicker foil makes channeling of the fragment cloud more severe, constraining its expansion to a higher degree than with the thinner foil honeycomb. In order to provide a quantitative estimate for the influence of honeycomb core foil thickness on dispersion of hypervelocity fragments, volumes occupied by the fragments at 10  $\mu$ s after impact initiation were roughly measured, as depicted in Figure 33. In simulation with the thicker foil, fragments occupied a volume of 1283 mm<sup>3</sup>, while when the thinner foil was used, the corresponding volume was twice as large (2541 mm<sup>3</sup>; see Figure 33). This confirms a significant influence of the honeycomb foil thickness on the channeling of debris cloud in HVI at normal incidence. As a result, panel with the thicker foil experienced full perforation, while no perforation was noted for the panel with the thinner honeycomb foil under the same impact conditions.

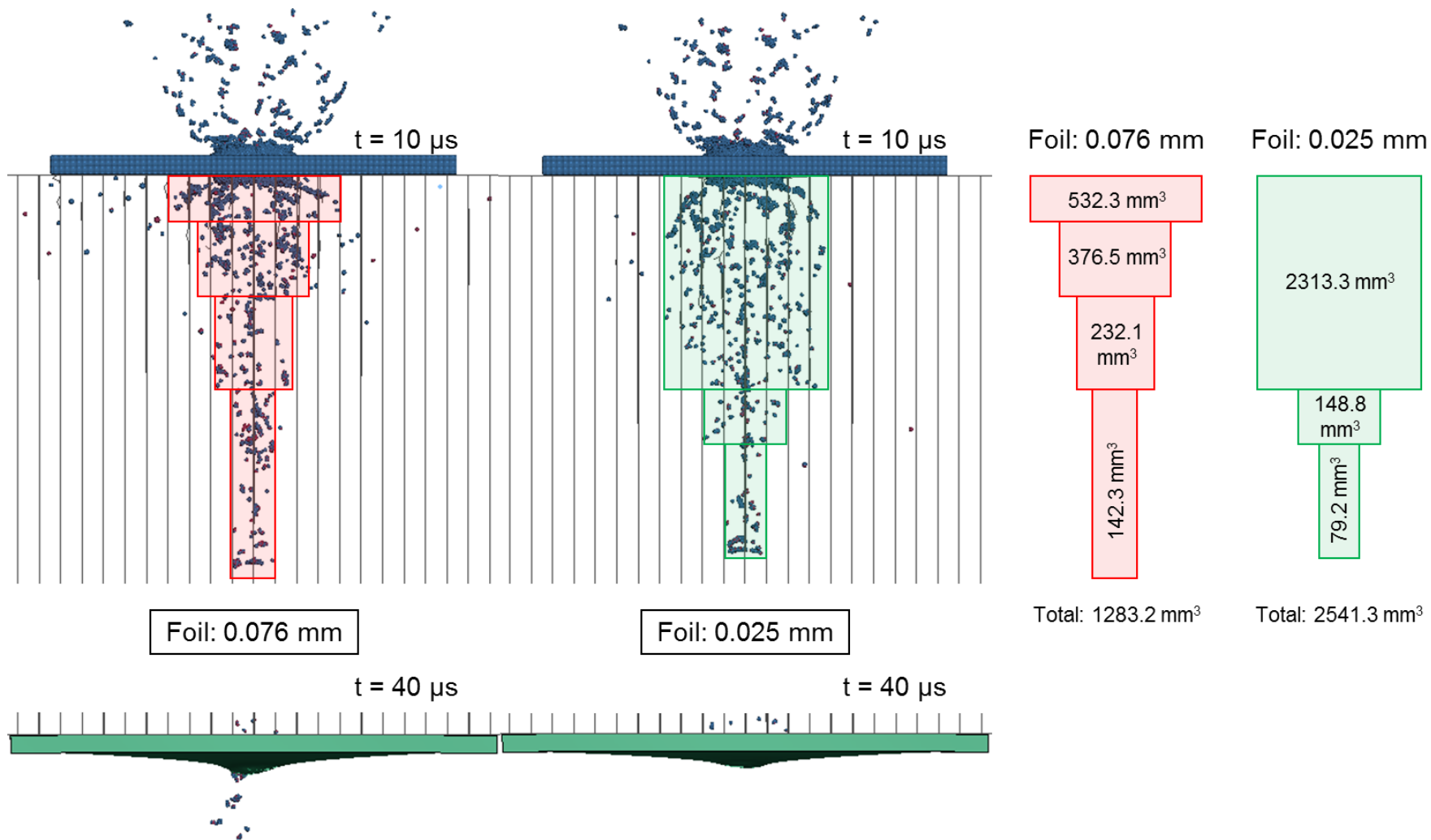


Figure 33 – Foil thickness effect on fragment cloud expansion and damage to the rear wall

### 3.4 Summary of Chapter 3

The developed simulation model was validated against the available experimental data (NASA HITF 9005 experiment) and against the predictions of the well-verified SRL ballistic limit equation.

After the validation, the model was used to investigate the effects of projectile shape in hypervelocity impact of honeycomb-core sandwich panels. The considered projectile topologies included spherical, disk-shaped, and ring-shaped impactors, with the latter two shapes represented by the projectiles with the aspect ratios of 1.5, 3.0, and 4.5.

Additional simulations were conducted and reported in this chapter to explore the effects of the honeycomb core. This included the effect of the honeycomb cell size (honeycombs with 1/8, 5/32, 3/16, and 1/4 inch cells were considered), the effect of projectile-honeycomb cell alignment (the “cell-center” alignment vs. the “wall” alignment), and the effect of the foil thickness (honeycombs with 0.076 mm and 0.025 mm-thick walls were considered).

Results of thirteen hypervelocity impact simulations with an overall computational time of around 600 hours have been reported in this chapter.

## 4: CONCLUSIONS AND FUTURE WORK

### 4.1 Conclusions

This study investigated projectile shape effects in hypervelocity impact of honeycomb-core sandwich structures. A model for hypervelocity projectile impact on a sandwich panel with a 50.8 mm-thick aluminum honeycomb and 1.3 mm-thick aluminum facesheets was developed and verified against available experimental data for the case of above-critical projectile, and using a well-validated ballistic limit equation – for near-critical spherical projectile impacts. The model then was used to simulate collisions with 7 km/s disk and ring-shaped impactors. The following conclusions can be drawn from the results of these analyses:

- When hit by disk-shaped projectiles with the aspect ratio from 1.5 to 4.5, no change to the ballistic limit of the panel was noted as compared to spherical projectile impacts.
- Simulated collisions with ring-shaped projectiles demonstrated a significant reduction of the panel's ballistic limit as compared to disk and spherical projectile impacts, which is an important finding of this study. It was estimated that a volume of a ring-shaped impactor needed to perforate the sandwich panel was 1.65 times smaller than that of a spherical projectile. Presently available predictive models for sandwich panels, such as the empirical BLE given by equation (19), do not account for projectile shape effects and, thus, may result in non-conservative predictions of ballistic limit.
- Aspect ratio of a ring projectile, varied from 1.5 to 4.5, affected the size of the exit hole in the panel's rear facesheet in a way that larger holes were predicted for smaller (1.5) and larger (4.5) aspect ratios, while smaller perforation size was predicted for the medium aspect ratio (3.0), suggesting the presence of several competitive mechanisms, which affect penetrating ability of ring projectiles when their aspect ratio is changed.
- Cell size was found to significantly affect the ballistic limit of honeycomb panels subjected by HVI at normal incidence. The increase of ballistic limit (simulation outcome changed from "perforation" to "no perforation") was achieved by simple replacement of 1/8 cell honeycomb by a honeycomb with the cell size of 3/16 inch, all other conditions being equal. It should be noted that presently existing ballistic limit

equations do not account for the cell size effect in hypervelocity impacts at normal incidence, which identifies the direction for their further improvement.

- Projectile/honeycomb cell alignment was found to affect the damage of the rear facesheet in case of HVI at normal incidence. Based on the results of this study, it is recommended to align a projectile with the honeycomb center in simulations that are conducted for design purposes in order to ensure that the most conservative scenario was explored. Similarly, in HVI experiments with honeycomb-core sandwich panels, when possible, it can be recommended to mark the position of honeycomb on internal side of the front facesheet prior to bonding the rear facesheet, and identify and report the position of projectile entry (e.g. “cell center”, “near wall”) after the post-mortem examination of the tested samples.
- Thickness of the honeycomb foil was found to have a noticeable influence on ballistic performance of HCSPs. It was found that severity of the channeling effect will reduce with the reduction of thickness of the foil, however, as certain amount of energy is absorbed through deformation of the honeycomb, there may exist a threshold after which further reduction of honeycomb thickness may not result in improvement of ballistic performance.

#### 4.2 Future work

The validated numerical model of HVI on HCSP developed in this study represents an economical and cost-efficient alternative to physical hypervelocity impact testing and is ready to be used in the design and analysis of orbital debris shielding of space satellites. Also, with minimal modifications, the developed model can be employed to investigate different previously unexplored or insufficiently studied impact scenarios and panel design configurations, including, but not limited to the following:

1. other projectile shapes and dimensions;
2. other projectile materials (e.g. plastic or steel projectiles);
3. other facesheet materials (e.g. titanium);
4. other panel configurations (e.g., double-core panels).

Another important area for future studies includes extending the applicability of the model to higher impact velocities (10 – 20 km/s). This would require the development and implementation of an equation of state that would account for phase transformations of the projectile and facesheet materials, as a significant portion of fragments can undergo melting and even vaporization at speeds exceeding 10 km/s.

With extensive use of composite materials in space structures, it can be expected that HCSP facesheets, honeycombs, as well as orbital debris itself, can be made of reinforced plastics (e.g., carbon fiber-reinforced epoxy). Modeling of such impact scenarios would require dedicated material models that can adequately represent the behavior of composites in collisions at orbital speeds, being another important direction for future studies.

## APPENDIX

### LS-DYNA MASTER FILE AND INCLUDES

#### **HCSP\_HVI\_MODEL.k:**

```
*KEYWORD MEMORY=800000000 MEMORY2=800000000 NCPU=8
*TITLE
$#
title
HCSP_HVI_MODEL
*INCLUDE_PATH
D:\SPECIFY A PATH TO THE FOLDER WITH THE "INCLUDES" HERE
*INCLUDE
$#
filename
Controls.k
*INCLUDE
$#
filename
Database.k
*INCLUDE
$#
filename
Parts.k
*INCLUDE
$#
filename
Sections.k
*INCLUDE
$#
filename
Contacts.k
*INCLUDE
$#
filename
Materials.k
*INCLUDE
```



```

$#
filename
PRJ_mesh_RING_1p9mm_0p95mm_0p42mm.k
*INCLUDE
$#
filename
FW_mesh_SPH.k
*INCLUDE
$#
filename
FW_mesh_Coarse_FEM.k
*INCLUDE
$#
filename
HC_mesh_01_3.18 mm_cell.k
$# HC_mesh_02_3.97 mm_cell.k
$# HC_mesh_03_4.76 mm_cell.k
$# HC_mesh_04_6.35 mm_cell.k
*INCLUDE
$#
filename
RW_mesh.k
*INCLUDE
$#
filename
Sets.k
*INCLUDE
$#
filename
Velocity.k
*END

```

### Controls.k:

```

*CONTROL_ACCURACY
$#      osu      inn      pidosu      iacc
          0          1          0          0
*CONTROL_BULK_VISCOSITY

```

\$#	q1	q2	type	btype	tstype				
	1.5	0.06	1	0	0				

\*CONTROL\_CONTACT

\$#	slsfac	rwpnal	islchk	shlthk	penopt	thkchg	orien	enmass	
	0.1	0.0	2	2	1	0	1	0	

\$#	usrstr	usrfrc	nsbcs	interm	xpene	ssthk	ecdt	tiedprj	
	0	0	0	0	4.0	0	0	0	

\$#	sfrc	dfrc	edc	vfc	th	th_sf	pen_sf		
	0.0	0.0	0.0	0.0	0.0	0.0	0.0		

\$#	ignore	frceng	skiprwg	outseg	spotstp	spotdel	spothin		
	0	0	0	0	0	0	0.0		

\$#	isym	nserod	rwgaps	rwgdth	rwksf	icov	swradf	ithoff	
	0	0	1	0.0	1.0	0	0.0	1	

\$#	shledg	pstiff	ithcnt	tdcnof	ftall	unused	shltrw	igactc	
	0	0	0	0	0		0.0	1	

\*CONTROL\_ENERGY

\$#	hgen	rwen	slnten	rylen	irgen				
	2	2	1	2	2				

\*CONTROL\_SHELL

\$#	wrpang	esort	irnxx	istupd	theory	bwc	miter	proj	
	20.0	0	-1	0	16	1	1	0	

\$#	rotascl	intgrd	lamsht	cstyp6	thshel				
	1.0	0	1	1	0				

\$#	psstupd	sidt4tu	cntco	itsflg	irquad	w-mode	stretch	icrq	
	0	0	0	0	2	0.0	0.0	0	

\$#	nfail1	nfail4	psnfail	keepcs	delfr	drcpsid	drcprm	intperr	
	1	1	0	0	0	0	1.0	0	

\*CONTROL\_SOLID

\$#	esort	fmatrix	nptets	swloc1	psfail	t10jtol	icohed	tet13k	
	0	1	4	1	0	0.0	0	0	

\$#	pm1	pm2	pm3	pm4	pm5	pm6	pm7	pm8	pm9	pm10
	0	0	0	0	0	0	0	0	0	0

\*CONTROL\_SPH

\$#	ncbs	boxid	dt	idim	nmneigh	form	start	maxv	
	1	01.00000E20		3	-85	0	0.0	10000.0	

```

$#      cont      deriv      ini      ishow      ierod      icon      iavis      isymp
          0          0          0          0          0          0          0          100

$#      ithk
          0

*CONTROL_TERMINATION

$#  endtim      endcyc      dtmin      endeng      endmas      nosol
      0.040          0      0.001      0.01.000000E8          0

*CONTROL_TIMESTEP

$#  dtinit      tssfacc      isdo      tslimt      dt2ms      lctm      erode      ms1st
      0.0          0.20          0          0.0          0.0          0          1          0

$#  dt2msf      dt2mslc      imsc1      unused      unused      rmsc1      unused      ihdo
      0.0          0          0          0          0          0.0          0          0

*END

```

### Database.k:

```

*DATABASE_ELOUT

$#      dt      binary      lcur      ioopt      option1      option2      option3      option4
      0.1          3          0          1          0          0          0          0

*DATABASE_GCEOUT

$#      dt      binary      lcur      ioopt
      0.1          3          0          1

*DATABASE_GLSTAT

$#      dt      binary      lcur      ioopt
      0.1          3          0          1

*DATABASE_MATSUM

$#      dt      binary      lcur      ioopt
      0.1          3          0          1

*DATABASE_NODFOR

$#      dt      binary      lcur      ioopt
      0.1          3          0          1

*DATABASE_RCFORC

$#      dt      binary      lcur      ioopt
      0.1          3          0          1

*DATABASE_SPCFORC

$#      dt      binary      lcur      ioopt

```

```

0.1      3      0      1

*DATABASE_BINARY_D3PLOT
$#      dt      lcdt      beam      npltc      psetid
2.50000E-4      0      0      0      0

$#      ioopt      rate      cutoff      window      type      pset
0      0.0      0.0      0.0      0      0

*DATABASE_BINARY_RUNRSF
$#      cycl      nr      beam      npltc      psetid
1000000.0      0      0      0      0

*DATABASE_EXTENT_BINARY
$#      neiph      neips      maxint      strflg      sigflg      epsflg      rltflg      engflg
0      16      16      1      1      1      1      1

$#      cmpflg      ieverp      beamip      dcomp      shge      stssz      n3thdt      ialemat
1      0      0      1      1      1      2      1

$#      nintsld      pkp_sen      sclp      hydro      msscl      therm      intout      nodout
0      0      1.0      0      0      0ALL      ALL

$#      dtdt      resplt      neipb      quadr      cubic
0      0      0      0      0

*DATABASE_EXTENT_INTFOR
$#      nglbv      nvelo      npresu      nshear      nforce      ngapc      nfail      ieverf
1      1      1      1      1      1      0      0

*END

```

## Parts.k:

```

*PART

$#                                          title

FW_Fine_SPHHHH

$#      pid      secid      mid      eosid      hgid      grav      adpopt      tmid
3      2      2      2      0      0      0      0

*PART

$#                                          title

SPH_PROJECTILE

$#      pid      secid      mid      eosid      hgid      grav      adpopt      tmid
5      2      1      1      0      0      0      0

*PART

```

```

$#                                     title
FW_Coarse_FEM
$#    pid    secid    mid    eosid    hgid    grav    adpopt    tmid
      7        1        2        2        0        0        0        0
*PART
$#                                     title
Singles
$#    pid    secid    mid    eosid    hgid    grav    adpopt    tmid
      9        3        5        0        0        0        0        0
*PART
$#                                     title
Doubblers
$#    pid    secid    mid    eosid    hgid    grav    adpopt    tmid
     10        4        5        0        0        0        0        0
*PART
$#                                     title
RW_Coarse_FEM
$#    pid    secid    mid    eosid    hgid    grav    adpopt    tmid
     11        1        6        2        0        0        0        0
*PART
$#                                     title
RW_Fine_FEM
$#    pid    secid    mid    eosid    hgid    grav    adpopt    tmid
     13        1        6        2        0        0        0        0
*DEFINE_ADAPTIVE_SOLID_TO_SPH_ID
$#    did                                     heading
      1RW_SOLID_TO_SPH
$#    ipid    itype    nq    ipsph    issph    icpl    iopt    cpcd
     13        0        1     14        2        1        1     0.0
*PART
$#                                     title
SPH_TO_CONVERT_SOLIDS_TO
$#    pid    secid    mid    eosid    hgid    grav    adpopt    tmid
     14        2        2        2        0        0        0        0
*END

```

## Sections.k:

\*SECTION\_SOLID\_TITLE

SOLID\_SECTION

\$#	secid	elform	aet
	1	1	0

\*SECTION\_SPH\_TITLE

SPH\_SECTION

\$#	secid	cslh	hmin	hmax	sphini	death	start	sphkern
	2	1.2	0.2	2.0	0.01.00000E20		0.0	2

\*SECTION\_SHELL\_TITLE

Singles\_HC

\$#	secid	elform	shrf	nip	propt	qr/irid	icomp	setyp
	3	16	1.0	3	1.0	0	0	1

\$#	t1	t2	t3	t4	nloc	marea	idof	edgset
	0.0762	0.0762	0.0762	0.0762	0.0	0.0	0.0	0

\*SECTION\_SHELL\_TITLE

Doubles\_HC

\$#	secid	elform	shrf	nip	propt	qr/irid	icomp	setyp
	4	16	1.0	3	1.0	0	0	1

\$#	t1	t2	t3	t4	nloc	marea	idof	edgset
	0.1524	0.1524	0.1524	0.1524	0.0	0.0	0.0	0

\*END

## Contacts.k:

\*CONTACT\_AUTOMATIC\_NODES\_TO\_SURFACE\_ID

\$#	cid	title						
	1FW_SPH__FW_FEM							

\$#	ssid	msid	sstyp	mstyp	sboxid	mboxid	spr	mpr
	2	1	4	0	0	0	0	0

\$#	fs	fd	dc	vc	vdc	penchk	bt	dt
	0.0	0.0	0.0	0.0	0.0	0	0.01.00000E20	

\$#	sfs	sfm	sst	mst	sfst	sfmt	fsf	vsf
	1.0	1.0	0.0	0.0	1.0	1.0	1.0	1.0

\$#	soft	sofscl	lcidab	maxpar	sbopt	depth	bsort	frcfrq
	1	0.1	0	1.025	2.0	2	0	1

\*CONTACT\_AUTOMATIC\_NODES\_TO\_SURFACE\_ID

\$#	cid	title
	2SPH_HONEYCOMB	

\$#	ssid	msid	sstyp	mstyp	sboxid	mboxid	spr	mpr
	4	5	2	2	0	0	0	0

\$#	fs	fd	dc	vc	vdc	penchk	bt	dt
	0.9	0.0	0.0	0.0	0.0	0	0.01.00000E20	

\$#	sfs	sfm	sst	mst	sfst	sfmt	fsf	vsf
	1.0	1.0	0.0	0.0	1.0	1.0	1.0	1.0

\$#	soft	sofscl	lcidab	maxpar	sbopt	depth	bsort	frcfrq
	1	0.1	0	1.2	2.0	2	0	1

\*CONTACT\_ERODING\_NODES\_TO\_SURFACE\_ID

\$#	cid	title
	3SPH_TO_RW_Fine	

\$#	ssid	msid	sstyp	mstyp	sboxid	mboxid	spr	mpr
	4	13	2	3	0	0	0	0

\$#	fs	fd	dc	vc	vdc	penchk	bt	dt
	0.9	0.0	0.0	0.0	0.0	0	9E-31.00000E20	

\$#	sfs	sfm	sst	mst	sfst	sfmt	fsf	vsf
	1.0000E-12	1.0000E-12	0.0	0.0	1.0	1.0	1.0	1.0

\$#	isym	erosop	iadj
	0	1	0

\$#	soft	sofscl	lcidab	maxpar	sbopt	depth	bsort	frcfrq
	1	0.1	0	1.025	2.0	2	0	1

\*CONTACT\_TIED\_NODES\_TO\_SURFACE\_OFFSET\_ID

\$#	cid	title
	4RW_Coarse_to_Fine	

\$#	ssid	msid	sstyp	mstyp	sboxid	mboxid	spr	mpr
	13	11	4	0	0	0	0	0

\$#	fs	fd	dc	vc	vdc	penchk	bt	dt
	0.0	0.0	0.0	0.0	0.0	0	0.01.00000E20	

\$#	sfs	sfm	sst	mst	sfst	sfmt	fsf	vsf
	1.0	1.0	0.0	0.0	1.0	1.0	1.0	1.0

\$#	soft	sofscl	lcidab	maxpar	sbopt	depth	bsort	frcfrq
	1	0.1	0	1.025	2.0	2	0	1

\*END

## Materials.k:

\*KEYWORD

\$#-----

\$#-----

\*EOS\_GRUNEISEN\_TITLE

AL2017-T4

\$#	eosid	c	s1	s2	s3	gamao	a	e0
	1	5328.0	1.338	0.0	0.0	2.00	0.00	0.0

\$#	v0	-	lcid
	1.0	0.0	0

\*MAT\_JOHNSON\_COOK\_TITLE

AL2017-T4

\$#	mid	ro	g	e	pr	dtf	vp	rateop
	1	0.002780	27480.0	73100.0	0.33	0.0	0.0	0.0

\$#	a	b	n	c	m	tm	tr	epso
	369.0	684.0	0.73	0.0083	1.70	925.0	293.0	0.001

\$#	cp	pc	spall	it	d1	d2	d3	d4
	885.0	-2000.0	1.0	0.0	9.00	0.00	0.00	0.0

\$#	d5	c2/p	erod	efmin	numint
	0.0	0.0	11.00000E-6	0.0	

\$#-----

\$#-----

\*EOS\_GRUNEISEN\_TITLE

EOS\_AL6061-T6

\$#	eosid	c	s1	s2	s3	gamao	a	e0
	2	5240.0	1.4	0.0	0.0	1.97	0.00	0.0

\$#	v0	-	lcid
	1.0	0.0	0

\*MAT\_JOHNSON\_COOK\_TITLE

STRENGTH\_AL6061-T6

\$#	mid	ro	g	e	pr	dtf	vp	rateop
-----	-----	----	---	---	----	-----	----	--------



	2	0.002703	26000.0	70000.0	0.3	0.0	0.0	0.0
\$#	a	b	n	c	m	tm	tr	epso
	324.0	114.0	0.42	0.002	1.34	925.0	293.0	0.001
\$#	cp	pc	spall	it	d1	d2	d3	d4
	885.0	-2000.0	1.0	0.0	9.00	0.00	0.00	0.0
\$#	d5	c2/p	erod	efmin	numint			
	0.0	0.0	11.00000E-6	0.0				
\$#	-----							
\$#	-----							
*MAT_PLASTIC_KINEMATIC_TITLE								
Al5052-HC_Shells								
\$#	mid	ro	e	pr	sigy	etan	beta	
	5	0.00268	70300.0	0.33	193.0	0.0	0.0	
\$#	src	srp	fs	vp				
	0.0	0.0	0.25	0.0				
\$#	-----							
\$#	-----							
*MAT_JOHNSON_COOK_TITLE								
AL6061-T6_RW								
\$#	mid	ro	g	e	pr	dtf	vp	rateop
	6	0.002703	26000.0	70000.0	0.3	0.0	0.0	0.0
\$#	a	b	n	c	m	tm	tr	epso
	324.0	114.0	0.42	0.002	1.34	925.0	293.0	0.001
\$#	cp	pc	spall	it	d1	d2	d3	d4
	885.0	-2000.0	1.0	0.0	9.00	0.00	0.00	0.0
\$#	d5	c2/p	erod	efmin	numint			
	0.0	0.0	11.00000E-6	0.0				
*MAT_ADD_EROSION								
\$#	mid	excl	mxpres	mneps	effeps	voleps	numfip	ncs
	6	0.0	0.0	0.0	0.250	0.0	1.0	1.0
\$#	mnpres	sigp1	sigvm	mxeps	epssh	sigth	impulse	failtm
	0.0	0.0	0.0	0.0	0.0	0.0	0.0	0.0
\$#	idam	-	-	-	-	-	-	lcregd
	0	0	0	0	0	0	0	0
\$#	lcfld	nsff	epsthin	engcrt	radcrt	lceps12	lceps13	lcepsmx

	0	10	0.0	0.0	0.0	0	0	0
--	---	----	-----	-----	-----	---	---	---

```

$#  dteflt      unused      mxtmp      dtmin
      0.0              0.0      0.0

*END

```

### PRJ\_mesh\_1p2mm.k:

```

*ELEMENT_SPH
$#  nid      pid      mass
    1299135      5  -9.920819e-04
    1299136      5  -9.920819e-04
.....
    1300046      5  -9.920819e-04

*NODE
$#  nid      x      y      z      tc      rc
    1299135     -0.55     -0.15     2.05     0     0
    1299136     -0.55     -0.15     2.15     0     0
.....
    1300046      0.55      0.15     2.35     0     0

*END

```

### FW\_mesh\_SPH.k:

```

*ELEMENT_SPH
$#  nid      pid      mass
    30721      3  2.703000e-06
    30722      3  2.703000e-06
.....
    1200720      3  2.703000e-06

*NODE
$#  nid      x      y      z      tc      rc
    30721     -14.95     -14.95     0.15     0     0
    30722     -14.95     -14.95     0.25     0     0
.....
    1200720     14.95004     14.95004     1.35     0     0

*END

```

### FW\_mesh\_Coarse\_FEM.k:

\*ELEMENT\_SOLID

\$#	eid	pid	n1	n2	n3	n4	n5	n6	n7	n8
	4901	7	1310848	1310849	1310920	1310919	1315889	1315890	1315891	1315892
	4902	7	1315889	1315890	1315891	1315892	1315893	1315894	1315895	1315896

.....

12900	7	1324143	1324145	1324287	1324285	1324144	1324146	1324288	1324286
-------	---	---------	---------	---------	---------	---------	---------	---------	---------

\*NODE

\$#	nid	x	y	z	tc	rc
	1310848	35.0	35.0	0.1	0	0
	1310849	34.0	35.0	0.1	0	0

.....

1324288	-35.0	-35.0	1.4	0	0
---------	-------	-------	-----	---	---

\*END

### HC\_mesh\_01\_3.18 mm\_cell.k:

\*ELEMENT\_SHELL

\$#	eid	pid	n1	n2	n3	n4	n5	n6	n7	n8
	3000000	10	3057614	3000002	3000006	3057616	0	0	0	0
	3000001	10	3000005	3057615	3057716	3000007	0	0	0	0

.....

3737663	10	3686851	3686735	3686737	3686852	0	0	0	0
---------	----	---------	---------	---------	---------	---	---	---	---

\*NODE

\$#	nid	x	y	z	tc	rc
	3000000	-6.14464	23.83	-50.8	0	0
	3000001	-5.68714	23.83	-50.8	0	0

.....

3686900	24.53741	3.16	-42.83137	0	0
---------	----------	------	-----------	---	---

\*END

### RW\_mesh.k:

\*ELEMENT\_SOLID

\$#	eid	pid	n1	n2	n3	n4	n5	n6	n7	n8
	6000000	11	6003816	6003817	6003818	6003819	6000000	6000001	6000072	6000071
	6000001	11	6003820	6003821	6003822	6003823	6003816	6003817	6003818	6003819
.....										
	7692007	13	7831235	7831248	7835941	7835928	7831234	7831247	7835940	7835927
*NODE										
\$#	nid		x		y		z		tc	rc
	6000000		35.0		35.0		-50.9		0	0
	6000001		34.0		35.0		-50.9		0	0
.....										
	7835941		-18.0		-18.0		-52.2		0	0
*END										

## Sets.k:

```
*SET_PART_LIST_TITLE
PS_FOR_ERODING_CONTACT_sphFW_sphPRJ
```

\$#	sid	da1	da2	da3	da4	solver				
	4	0.0	0.0	0.0	2.0MECH					

\$#	pid1	pid2	pid3	pid4	pid5	pid6	pid7	pid8
	3	5	0	0	0	0	0	0

```
*SET_PART_LIST_TITLE
PS_FOR_ERODING_CONTACT_HCingles_HCdoublers
```

\$#	sid	da1	da2	da3	da4	solver				
	5	0.0	0.0	0.0	2.0MECH					

\$#	pid1	pid2	pid3	pid4	pid5	pid6	pid7	pid8
	9	10	0	0	0	0	0	0

```
*SET_SEGMENT_TITLE
FW_Coarse_FEM_Perimeter
```

\$#	sid	da1	da2	da3	da4	solver				
	1	0.0	0.0	0.0	0.0MECH					

\$#	n1	n2	n3	n4	a1	a2	a3	a4
	1321537	1321539	1321535	1321533	0.0	0.0	0.0	0.0
	1320342	1320258	1320260	1320344	0.0	0.0	0.0	0.0
	1319751	1319835	1319836	1319752	0.0	0.0	0.0	0.0
	1320090	1320006	1320008	1320092	0.0	0.0	0.0	0.0

1321541	1321543	1321539	1321537	0.0	0.0	0.0	0.0
.....							
1320594	1320510	1320512	1320596	0.0	0.0	0.0	0.0
1320003	1320087	1320088	1320004	0.0	0.0	0.0	0.0
*SET_NODE_LIST_TITLE							
FW_Fine_SPH_Perimeter							
\$#	sid	da1	da2	da3	da4	solver	
	2	0.0	0.0	0.0	0.0	MECH	
\$#	nid1	nid2	nid3	nid4	nid5	nid6	nid8
	34608	34609	34610	34611	34612	34613	34615
	34616	34617	34618	34619	34620	38508	38510
	38511	38512	38513	38514	38515	38516	38518
	38519	38520	42408	42409	42410	42411	42413
	42414	42415	42416	42417	42418	42419	46308
.....							
1200696	1200697	1200698	1200699	1200700	1200701	1200702	1200703
1200704	1200705	1200706	1200707	0	0	0	0
*SET_NODE_LIST_TITLE							
RW_Fine_Perimeter_Nodes							
\$#	sid	da1	da2	da3	da4	solver	
	13	0.0	0.0	0.0	0.0	MECH	
\$#	nid1	nid2	nid3	nid4	nid5	nid6	nid8
	6011448	6011449	6011450	6011451	6011452	6011453	6011455
	6011456	6011457	6011458	6011459	6011460	6011461	6011463
	6011464	6011465	6011466	6011467	6011468	6011469	6011471
	6011472	6011473	6011474	6011475	6011476	6011477	6011479
	6011480	6011481	6011482	6011483	6011484	6011485	6011487
.....							
6967758	6967760	6967762	6972431	6972433	6972435	6972437	6972439
6972441	6972443	6972445	6972447	6972449	6972451	6972453	6972455
*SET_SEGMENT_TITLE							
RW_Coarse_Perimeter_Nodes							
\$#	sid	da1	da2	da3	da4	solver	
	11	0.0	0.0	0.0	0.0	MECH	
\$#	n1	n2	n3	n4	a1	a2	a4

6009002	6009000	6008926	6008927	0.0	0.0	0.0	0.0
6008854	6008926	6002555	6002519	0.0	0.0	0.0	0.0
6008931	6008929	6009136	6009138	0.0	0.0	0.0	0.0
6009000	6002556	6002555	6008926	0.0	0.0	0.0	0.0
6009004	6002557	6002556	6009000	0.0	0.0	0.0	0.0
.....							
6006623	6006695	6006694	6006622	0.0	0.0	0.0	0.0
6006699	6006627	6006625	6006697	0.0	0.0	0.0	0.0

\*END

### Velocity.k:

\*INITIAL\_VELOCITY\_GENERATION

\$#nsid/pid	styp	omega	vx	vy	vz	ivatn	icid
5	2	0.0	0.0	0.0	-6910.0	0	0
\$#	xc	yc	zc	nx	ny	nz	phase
0.0	0.0	0.0	0.0	0.0	0.0	0	1

\*END

## REFERENCES

1. <https://orbitaldebris.jsc.nasa.gov/faq/>
2. [https://www.nasa.gov/mission\\_pages/station/news/orbital\\_debris.html](https://www.nasa.gov/mission_pages/station/news/orbital_debris.html)
3. E. L. Christiansen (NASA/Johnson Space Center, “Handbook for Designing MMOD Protection”, Astromaterials Research and Exploration Science Directorate ( KA ), Human Exploration Science Office ( KX ), NASA Johnson Space Center ( JSC ),” 2009.
4. A. Cherniaev, “Design And Analysis of Orbital Debris Protection For Spacecraft Composite Pressure Vessels”, PhD thesis, University of Manitoba, Winnipeg, 2016.
5. Orbital Debris: A Technical Assessment, *National Academies Press*, 1995.
6. E. L. Christiansen. "Meteoroid/Debris Shielding", 2003.
7. A. Cherniaev and I. Telichev, “Weight-Efficiency of Conventional Shielding Systems in Protecting Unmanned Spacecraft from Orbital Debris,” *Journal of Spacecraft and Rockets*. 54(1): 75-89, 2016.
8. Protecting the Space Station from Meteoroids and Orbital Debris. *National Academies Press*, 1997.
9. E.L. Christiansen, K. Nagy, D. M. Lear, and T. G. Prior. “Space Station MMOD Shielding”. *Acta Astronautica* 65 (7-8), Elsevier BV: 921-29, 2009.
10. R. Destefanis, F. Schafer, M. Lambert, M. Faraud, and E. Schneider, “Enhanced Space Debris Shields for Manned Spacecraft”, *International Journal of Impact Engineering*, 29(1-10), Elsevier BV: 215-26, 2003.
11. Akahoshi, Yasuhiro, R. Nakamura and M. Tanaka, “Development of Bumper Shield Using Low Density Materials”, *International Journal of Impact Engineering*, 26(1-10), Elsevier BV: 13-19, 2001.
12. F. L. Whipple, “Meteorites and Space Travel,” *The Astronomical Journal* 52. IOP Publishing: 131, 1947.
13. E. L. Christiansen, “Design and Performance Equations for Advanced Meteoroid and Debris Shields”. *International Journal of Impact Engineering* 14(1-4), Elsevier BV: 145-56, 1993.

14. E. L. Christiansen, J. L. Crews, J. E. Williamsen, J.H. Robinson, and A. M. Nolen, "Enhanced Meteoroid and Orbital Debris Shielding", *International Journal of Impact Engineering* 17(1-3), Elsevier BV: 217-228, 1995.
15. R. Destefanis, M. Faraud, and M. Trucchi, "Columbus Debris Shielding Experiment and Ballistic Limit Curves", *International Journal of Impact Engineering* 23(1), Elsevier BV: 181-92, 1999.
16. S. Ryan, E. L. Christiansen, "Micrometeoroid and Orbital Debris (MMOD) Shield Ballistic Limit Analysis Program", NASA/TM-2009-214789, 2010.
17. Protection Manual, Inter-Agency Space Debris Coordination Committee, IADC- 04-03, 2011.
18. D. O. Adams, et al, "Multi-Functional Sandwich Composites for Spacecraft Applications: An Initial Assessment", NASA/CR-214880, 2007.
19. L. A. Bylander, O. H. Carlstrom, T. S. R Christenson, and F. G. Olsson, "A Modular Design Concept for Small Satellites", *In Smaller Satellites: Bigger Business?*, 357-58. Springer Netherlands, 2002.
20. I. Telichev and A. Cherniaev, "Hypervelocity Impact Simulations on the "ENSURE" concepts for MMOD Protection" – Milestone Report for Space Technology Development Program "STDP" Project – Design of Novel MMOD Shield Technologies, submitted to Magellan Aerospace. 89. The University of Manitoba, 2015.
21. I. Telichev and A. Cherniaev, "Hypervelocity Impact Experiments on the "ENSURE" panels and filament- wound composites" – Milestone Report for Space Technology Development Program "STDP" Project – Design of Novel MMOD Shield Technologies, submitted to Magellan Aerospace. 66. The University of Manitoba, 2015.
22. R. Destefanis, F. Schafer, "Hypervelocity Impact Testing of CFRP/AL Honeycomb Satellite Structures. In *Proc. of the 4th European Conference on Space Debris* (ESA SP-587), 2005.
23. J. M. Sibeaud, L. Thamié, and C. Puillet, "Hypervelocity Impact on Honeycomb Target Structures: Experiments and modeling," *Int. J. Impact Eng.*, vol. 35, no. 12, pp. 1799–1807, 2008.



24. S. J. Ryan, E. L. Christiansen, D. M. Lear, M. Elert, M. D. Furnish, W. W. Anderson, W. G. Proud, and W. T. Butler, "Development of the Next Generation of Meteoroid and Orbital Debris Shields", In: *AIP Conference Proceedings*, Vol. 1195, 2010.
25. S. Ryan, T. Hedman and E. L. Christiansen, "Honeycomb vs. Foam: Evaluating Potential Upgrades to ISS Module Shielding", *Acta Astronautica* 67(7-8). Elsevier BV: 818-25, 2010.
26. B. Lathrop, and R. Sennett, "The Effects of Hypervelocity Impact on Honeycomb Structures", In *9<sup>th</sup> Structural Dynamics and Materials Conference*. American Institute of Aeronautics and Astronautics, 1968.
27. E. A. Taylor, M. K. Herbert, B. A. M. Vaughan, and J. A. M. McDonnell, "Hypervelocity Impact on Carbon Fiber Reinforced Plastic / Aluminum Honeycomb: Comparison with Whipple Bumper Shields", *International Journal of Impact Engineering* 23(1). Elsevier BV: 883-93, 1999.
28. S. Ryan, F. Schaefer, R. Destefanis, and M. Lambert, "A Ballistic Limit Equation for Hypervelocity Impacts on Composite Honeycomb Sandwich Panel Satellite Structures", *Advances in Space Research* 41(7), Elsevier BV: 1152-66, 2008.
29. C. Frost and P. Rodriguez, "AXAF Hypervelocity Impact Test Results", In *Second European Conference on Space Debris*, organized by ESA, Held 17-19 March, 1997, ESOC, Darmstadt, Germany.
30. M. J. Carrasquilla and J. E. Miller, "Shape Effect Analysis of Aluminum Projectile Impact on Whipple Shields," *Procedia Eng.*, vol. 204, pp. 308–314, 2017.
31. F. K. Schafer, M. Herrwerth, S. J. Hiermaier, and E. E. Schneider, "Shape Effects in Hypervelocity Impact on Semi-Infinite Metallic Targets," *International Journal of Impact Engineering*, vol 26, 699-711, 2001.
32. X. Liu, F. Gai, and S. Cheng, "Numerical Simulation on Characteristics of Debris Clouds Produced by Conical Projectiles Hypervelocity Impact on Thin Plates," *International Journal of Hybrid information Technology*, vol. 8, no. 6, pp. 79–86, 2015.
33. R. Vignjevic, J. C. Campbell, A. Monthienthong, U. Kingdom, and U. Kingdom, "Geometrical Shapes of Projectiles Effect on Hypervelocity Impact," no. July, pp. 5–9, 2009.

34. M. V. Silnikov, I. V. Guk, A. I. Mikhaylin, A. F. Nechunaev, and B. V. Rumyantsev, "Numerical Simulation of Hypervelocity Impacts of Variously Shaped Projectiles with Thin Bumpers," *Materials Physics and Mechanics*, vol. 42, pp. 20–29, 2019.
35. R. H. Morrison, "A Preliminary Investigation of Projectile Shape Effects in Hypervelocity Impact of a Double-Sheet Structure," no. August, 1972.
36. A. J. Piekutowski, "Debris Clouds Produced by the Hypervelocity Impact of Nonspherical Projectiles", *International Journal of Impact Engineering*, vol 26, 613-624, 2001.
37. K. Hu and W. P. Schonberg, "Ballistic Limit Curves for Cylindrical Projectiles Impacting Dual-Wall Spacecraft Systems," *Structures and Materials*, vol. 11. pp. 101–109, 2002.
38. W. P. Schonberg and J. E. Williamsen, "RCS-Based Ballistic Limit Curves for Non-Spherical Projectiles Impacting Dual-Wall Spacecraft Systems," *International Journal of Impact Engineering*, vol 33, pp. 763–770, 2006.
39. L.C. Chhabildas, E.S. Hertel, S.A. Hill, "Hypervelocity Impact Tests and Simulations of Single Whipple Bumper Shield Concepts at 10 km/s," *Int. J. Impact Engng*, 14: 133-144, 1993.
40. J. E. Miller, Considerations of Oblique Impacts of Non-Spherical, Graphite-Epoxy Projectiles," *First Int'l. Orbital Debris Conf*, 2019.
41. P. Kang, S. K. Youn, and J. H. Lim, "Modification of The Critical Projectile Diameter of Honeycomb Sandwich Panel Considering The Channeling Effect in Hypervelocity Impact," *Aerosp. Sci. Technol.*, vol. 29, no. 1, pp. 413–425, 2013.
42. Iliescu, L. E. Lakis, A. A. & Oulmane, A, "Sattelites/Spacecraft Materials And Hypervelocity Impact (HVI) Testing: Numerical Simulations," *Journal, M. Engineering, E. Centre, and D. Uk*, vol. 4, no. 1, pp. 24–64, 2017.
43. M. Schubert, S. Perfetto, A. Dafnis, D. Mayer, H. Atzrodt, K. U. Schroder, "Multifunctional Load Carrying Lightweight Structures For Space Design," *Institute of Structural Mechanics and Lightweight Design , RWTH Aachen University , Fraunhofer Institute for Structural Durability and System Reliability LBF , Darmstadt* , pp. 1–11, 2017.
44. C. J. Hayhurst, J. H. Ranson, D. J. Gardner and N. K. Birnbaum, "Modelling Of

- Microparticle Hypervelocity Oblique Impacts On Thick Targets,” International Journal of Impact Engineering, Vol. 17, pp. 375-386, 1995.
45. Stellingwerf R.F., Wingate C.A., “Impact Modeling With Smooth Particle Hydrodynamics,” Int. J. Impact Eng., 14 (1), pp. 707-718, 1993.
  46. F. A. Allahdadi, T. C. Carney, J. R. Hipp, L. D. Libersky, A. G. Petschek, “High Strain Lagrangian Hydrodynamics: A Three-Dimensional SPH Code For Dynamic Material Response,” Phillips Laboratory, PL-TR-92-1054, 1992.
  47. K. Shintate, H. Sekine, “Numerical Simulation Of Hypervelocity Impacts Of A Projectile On Laminated Composite Plate Targets By Means Of Improved SPH Method. Composites,” Part A, 35, 683–692, 2004.
  48. F. Xu, Y. Zhao, Y. Li, M. Kikuchi, “Study Of Numerical And Physical Fracture With SPH Method,” Acta Mechanica Solida Sinica, Vol. 23, 2010.
  49. G. Pezzica, R. Destefanis, M. Faraud, “Numerical Simulation of Orbital Debris Impact On Spacecraft,” In: International Conference on Structures under Shock and Impact, SUSI. 275-284, 1996.
  50. C. J. Hayhurst, R. Clegg, “Cylindrically Symmetric SPH Simulations of Hypervelocity Impacts On Thin Plates,” Int. J. Impact Eng. 20, 337 – 348, 1997.
  51. C. J. Hayhurst, I. H. Livingstone, R. Clegg, G. E. Fairlie, S. J. Hiermaier, M. Lambert, “Numerical Simulation of Hypervelocity Impacts On Aluminum And Nextel/Kevlar Whipple Shields,” In: Proceedings of Hypervelocity Shielding Workshop, 8 - 11 March 1998, Galveston, Texas.
  52. Y. Michel, J. M. Chevalier, C. Durin, C. Espinosa, F. Malaise, J. J. Barrau, “Hypervelocity Impacts On Thin Brittle Targets: Experimental Data And SPH Simulations,” Int. J. Impact Eng. 33, 441 – 451, 2006.
  53. R. A. Clegg, D. M. White, W. Riedel, W. Harwick, “Hypervelocity Impact Damage Predictions In Composites: Part I - Material Model And Characterization”, Int. J. Impact Eng. 33, 190 – 200, 2006.
  54. D. Palmeri, F. Schaefer, S. Hiermaier, M. Lambert, “Numerical Simulation of Non-Perforating Impacts On Shielded Gas-Filled Pressure Vessels,” Int. J. Impact Eng. 26, 591 – 602, 2001.
  55. Selected Hugoniot, Los Alamos Scientific Laboratory, 1969.

56. M. A. Meyers, "Dynamic Behavior of Materials," John Wiley & Sons, Inc., Hoboken, NJ, USA, 1994.
57. G. Kay, "DOT/FAA/AR-03/57: Failure Modeling of Titanium 6Al-4V and Aluminum 2024-T3 with the Johnson-Cook Material Model," Lawrence Livermore National Laboratory, Livermore, 2003.
58. D. R. Lesuer, G.J. Kay and M. M. LeBlanc "Modeling Large-Strain, High-Rate Deformation In Metals," in Engineering Research, Development and Technology, 1999.
59. T. Legaud, M. Le Garrec, N. Van Dorsselaer, V. Lapoujadet, "Improvement of Satellites Shielding Under High Velocity Impact Using Advanced SPH Method," 12th European LS-DYNA Conference, 2019, Koblenz, Germany.
60. Steinberg D., Equations of state and strength properties of selected materials. Lawrence Livermore National Laboratory, 1996.
61. S. Ryan, E. Christiansen, "Hypervelocity Impact Testing Of Aluminum Foam Core Sandwich Panels. NASA/TM-2015-218593.
62. LS-DYNA, Keyword user's manual volume I, Livermore Software Technology Corporation (LSTC), 2013.
63. HexWeb® CR III: Corrosion Resistant Specification Grade Aluminum Honeycomb. Hexcel Product Data Sheet. [www.hexcel.com](http://www.hexcel.com)
64. W. Jolly and W. P. Schonberg, "Analytical Prediction of Hole Diameter in Thin Plates Due to Hypervelocity Impact of Spherical Projectiles," Shock and Vibration, vol. 4, no. 5,6, pp. 379-390, 1997

## VITA AUCTORIS

NAME: Reihaneh Aslebagh

PLACE OF BIRTH: Tehran, Iran

YEAR OF BIRTH: 1992

EDUCATION: Narjes High School, Tehran, Iran, 2011

Khaje Nasir Toosi University of Technology,  
B.Sc., Tehran, Iran, 2016

University of Windsor, M.A.Sc., Windsor, ON,  
2021